



ΠΑΝΕΠΙΣΤΗΜΙΟ ΚΡΗΤΗΣ
UNIVERSITY OF CRETE

Department of Physics

Undergraduate Dissertation

Optoelectronic properties of WS₂/graphene heterostructures

Christos Paspalides

Supervisor: Prof. George Kioseoglou

June 2020

Abstract

During the last decade, the interest in investigating two dimensional materials was rapidly increased. Particularly, a class of materials known as Transition Metal Dichalcogenides (TMDs) exhibit promising properties in their two-dimensional form, making them attractive for future fundamental studies and applications. Some challenges considering the isolation and identification of TMD monolayers have been dealt through the introduction of a standard spectroscopic set of techniques such as Raman, Absorbance and Photoluminescence. For the last couple of years many studies have been focused in the examination of WS₂/graphene heterostructures in order to explore their optoelectronic properties.

The aim of this dissertation is two-fold. Firstly, the fabrication of the heterostructure samples was carried out using mechanical exfoliation for isolating WS₂ monolayers and few-layer graphene flakes. The exfoliated flakes were subsequently identified and characterized using optical microscopy and a combination of the three spectroscopic techniques. Additionally, a deterministic transfer setup was used for the stamping procedure in combination with the annealing treatment of samples. The importance of annealing for the coupling of the layers was confirmed and highlighted throughout the project. The second goal of this work was the spectroscopic study of the excitonic properties of WS₂/graphene heterostructures, which are strongly correlated with their optoelectronic properties. Therefore, the optical response of the sandwiched sample was examined under temperature dependent Photoluminescence in the range of 78K-300K.

Acknowledgements

I sincerely thank Prof. George Kioseoglou and George Kourmoulakis for devoting time towards my personal and academic development. During unprecedented challenges due to coronavirus pandemic we managed to continue this project and get valuable results. Their constant support and contribution were decisive for the completion of my undergraduate thesis. Finally, I'm grateful to Dr. Emmanuel Stratakis for allowing me to work with his experimental setup and to all the members of the Lab for their collaboration.

Contents

Abstract

Acknowledgements

Contents

I. Introduction

1. Theoretical background of WS₂ and graphene structures

- 1.1 Graphene – structure and properties
- 1.2 Two-dimensional single layer of WS₂
 - 1.2.1 Crystal Structure
 - 1.2.2 Brillouin zone and Electronic Band Structure
 - 1.2.3 Electronic structure of WS₂/graphene heterostructures
 - 1.2.4 Optical Properties – Excitons in WS₂ monolayers

2. Theory of Raman and Photoluminescence Spectroscopy

- 2.1 Raman Spectroscopy
- 2.2 Phonon Dispersion of monolayer WS₂ and graphene
- 2.3 Photoluminescence Spectroscopy
- 2.4 Photoluminescence and Differential Reflectance Spectroscopy of monolayer WS₂

II. Experimental Methods and Results

3. Experimental Methods

- 3.1 Optical Setup
 - 3.1.1 micro-PL configuration
 - 3.1.2 micro-R configuration
- 3.2 Cryogenic System
- 3.3 Sample preparation
 - 3.3.1 Sample definition

4. Experimental Results and Discussion

- 4.1 Spectroscopic study of samples
- 4.2 Annealing procedure
- 4.3 Spectroscopic study of samples after the annealing treatment
- 4.4 T-dependent photoluminescence

5. Summary and future work

III. REFERENCES

Part I

Introduction

Theoretical background of graphene and WS₂ structures

1.1 Graphene – structure and properties

Graphene is one of the most important and well-studied materials of the modern technological era. It is the forerunner of a new family of materials, known as “two-dimensional materials”. Its special set of mechanical, optical and electrical properties constitutes a powerful weapon for fundamental study and technological applications.

The lattice structure of graphene consists of a single layer of carbon atoms which are covalently connected in a honey-comb formation (Figure 1.1a). Every carbon atom is connected with each other by three in plane σ -bonds, while the remaining π orbital is out-of-plane.

The electronic properties of graphene arise from its unique electronic band structure. The empty conduction band touches the filled valence band at the K, K' (Dirac Points) of the First Brillouin zone, as shown in Figure 1.1b. Graphene's electronic band structure shows its semi-metallic behavior, because of the zero-energy gap at the Dirac points [1]. The level of Fermi energy lies at the K, K' points, which results in high carrier mobilities ($\sim 2 \times 10^5$ cm²/V.sec) and extraordinary electrical conductivity. Graphene also possesses some interesting optical properties such as negligible reflectance (<1%) and great transparency (97.3%) [2].

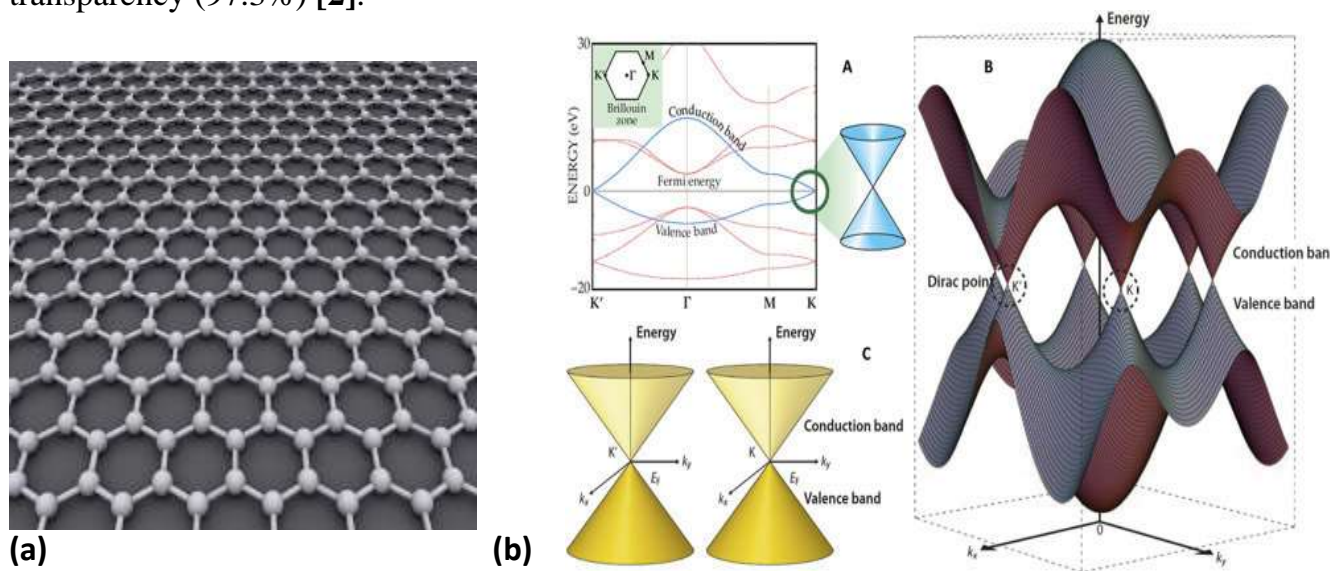


Fig1.1: a) The honey-comb lattice structure and b) First Brillouin zone of graphene [3].

1.2 Two-dimensional single layer of WS₂

Material tungsten disulfide (WS₂) belongs in the family of Transition Metal Dichalcogenides (TMDs) with the generic formula MX₂, where M stands for a Metal atom and X for a chalcogen. These two-dimensional (2D) materials present some interesting properties at the single layer limit, where they exhibit an indirect to direct transition crossover [4]. The enhanced photoluminescence of single layer 2D materials combined with atomic-scale thicknesses suggest that they could be a good candidate for future technological applications.

1.2.1 Crystal Structure

Tungsten disulfide adopts a layered structure shown in Figure 1.2 [5], where one atomic layer of W atoms is sandwiched by two atomic layers of S. These layers form W-S covalent bonds and the W atom lies at the center of trigonal-prismatic geometry formed by six S atoms [6]. The typical thickness for such quasi-2D layer is 6-7 Å.

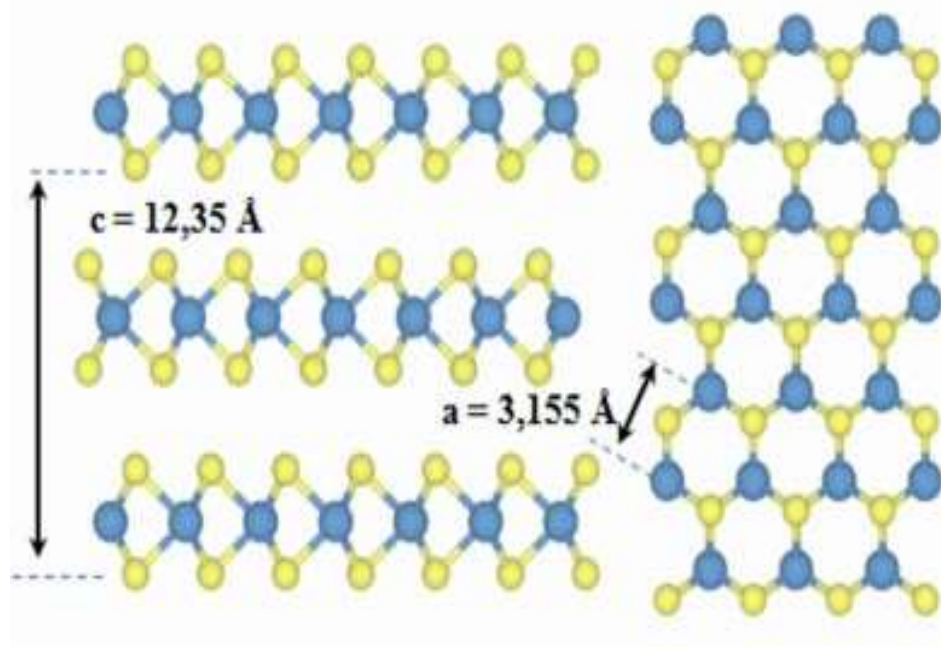


Figure 1.2: Schematic of WS₂ structure with lattice parameters a, c indicated. Blue spheres represent the W atom and yellow spheres stand for S atom.

In the trigonal-prismatic formation the two chalcogenides are stacked directly above each other resulting in a hexagonal (H) symmetry (Figure 1.3). The most commonly found coordination phases for a single-layered TMD are prismatic and octahedral [7]. Three examples of such polymorphs are 1T, 2H, 3R, where the digit represents the number of layers in the unit cell and the letter indicates the symmetry.

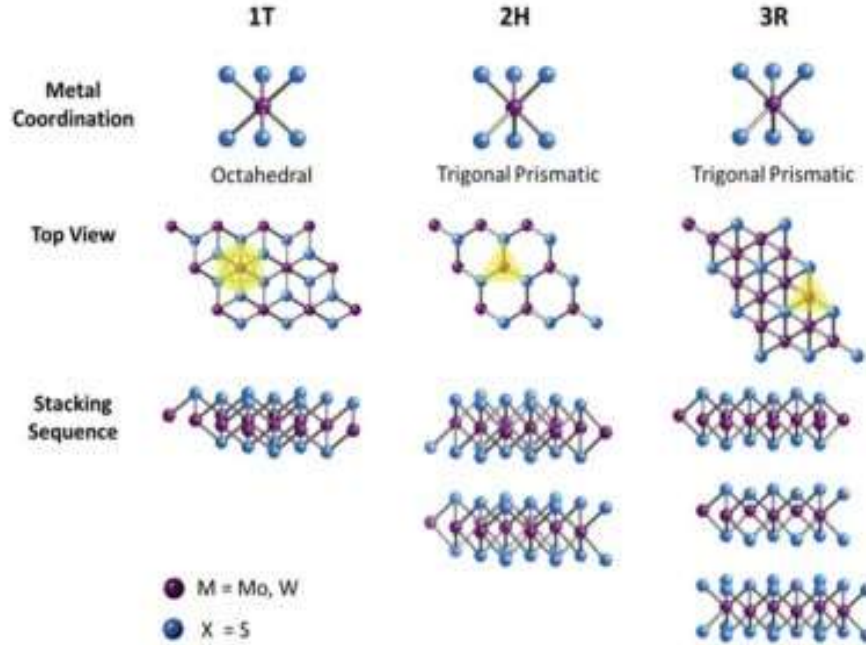


Figure 1.3: Schematic of coordination phases and stacking sequences of TMDs.

1.2.2 Brillouin zone and electronic band structure

Low dimensional materials with hexagonal lattice structures have two degenerate, yet inequivalent K, K' points located at the edge of Brillouin zone [8]. Those high symmetry points are usually a local maximum in the valence band and a local minimum in the conduction band with a splitting magnitude of approximately 0.4eV [9]. Figures 1.4a and 1.4b illustrate the unit cell of a single layer and the first Brillouin zone of WS₂. The electronic band structure of monolayer and five-layer WS₂ depicts a direct energy band gap (~2 eV) (Figure 1.4c) for the former and an indirect one for the later (Figure 1.4d). The indirect to direct transition for a multilayered or bulk WS₂ to monolayer WS₂ derives from quantum confinement effects [10].

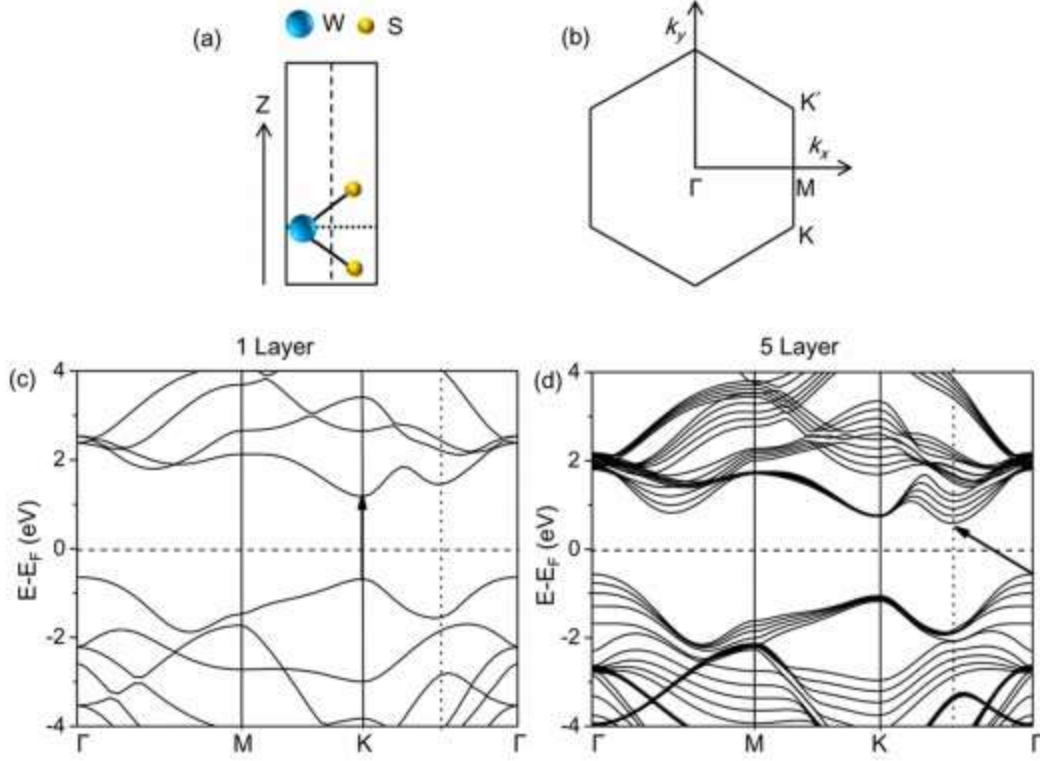


Figure 1.4: a) 3D view of the 1H-WS₂ unit cell. b) The first Brillouin zone of single layer WS₂, with high symmetry points denoted. E-k diagrams (DFT calculations) for c) 1 Layer and d) 5 Layer WS₂. Bold arrows indicate the direct and indirect transitions respectively.

1.2.3 Electronic structure of WS₂/graphene heterostructures

Thanks to their weak interlayer coupling, 2D materials such as WS₂ and graphene can be vertically stacked to form van der Waals heterostructures. Such heterostructures gain different properties than those of each individual 2D material [11]. Particularly, monolayer TMD/graphene stacks are van der Waals heterostructures of interest since they combine the high carrier mobility of graphene, as well as the strong light-matter interactions of single layer TMD [12].

The interlayer distance between the graphene layer and the 2D material layer can be very small, therefore interlayer interactions beyond London dispersion are apparent, leading to modification of optical absorption and band structures [13]. Furthermore, interlayer interactions (e.g. interlayer excitons) have been a subject of recent scientific interest, as they contribute to interfacial charge generation and separation [14].

According to Yuan et al, a two-model electronic band structure calculation has been performed for the 1L-WS₂/graphene heterostructure. The aim of the project was to identify possible interlayer transitions. Figure 1.5 [14] shows the energy band structure of WS₂/graphene heterostructure calculated using density functional theory (DFT). The commensurate model considers a small mismatch (2,3%) between the lattice vectors of WS₂ and graphene supercells, whereas the incommensurate model accounts for a large lattice mismatch of about 22%. The corresponding band structure (Figure 1.5A) is an almost perfect superposition of the two individual band structures of graphene and WS₂. It is apparent from the diagram that the conduction band of WS₂ is located at about 1eV above the Dirac point (K) of graphene. On the other hand, Figure 1.5B was obtained after calculating the separate perfect monolayers and then plotting their band structure as an overlap, with the shift of the band edges calculated in the previous step.

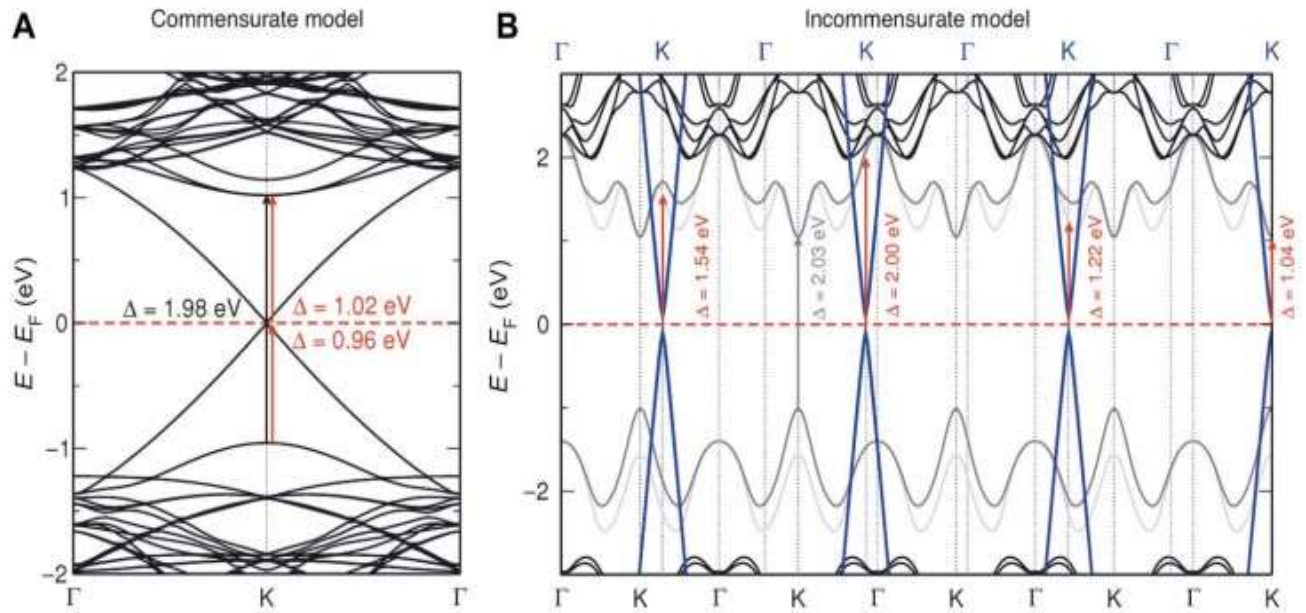


Figure 1.5: Band structure of the WS₂/graphene heterostructure. A) Commensurate model of a 5×5 graphene/ 4×4 WS₂ supercell. B) Incommensurate model of corresponding perfect unit cells (as in a single layer) of each component along the Γ -K direction. Fermi energy is drawn as a red dotted line. The red arrows represent interlayer transitions.[14]

1.2.5 Optical Properties – Excitons in WS₂ monolayers

As discussed in section 1.2 2D materials exhibit an indirect to direct transition crossover when reaching the single layer limit. Apart from enhanced photoluminescence, many other interesting properties arise from reduced dimensionality. In WS₂ monolayers, breaking the inversion symmetry leads to strong spin-orbit coupling which results in the splitting of valence bands at K, K' points with a sub-gap of around 0.4 eV [15]. Also, the split spins at the K and K' valleys have the opposite signs. Thus, such spin–valley coupling offers an extra degree of freedom to charge carriers in WS₂ monolayers. Many theoretical predictions and experiments have reported a non-equilibrium charge carrier imbalance at two valleys, revealed by the difference of absorption of left-(σ^-) and right-handed (σ^+) circular polarized lights at the two valleys [16]. The aforementioned optical properties suggest that WS₂ could be a good candidate for future nanoelectronics, spintronics, valleytronics, and optoelectronics.

Excitons play a crucial role not only in the electronic properties of TMDs, but also determine the nature of their optical properties. Hence, it is important to gain a better understanding of excitons and their behavior in such two-dimensional systems. The absorption of a photon by an interband transition in a semiconductor creates an electron in the conduction band and a hole in the valence band. The oppositely charged particles are created at the same point in space and can attract each other through their mutual Coulomb interaction. This attractive interaction favors the formation of an electron-hole pair, and therefore increases the optical transition rate. Finally, if the right conditions are satisfied, a neutral, bound electron-hole pair can be formed, known as neutral exciton. Figure 1.6 presents the two types of excitons that can be found in solids [17].

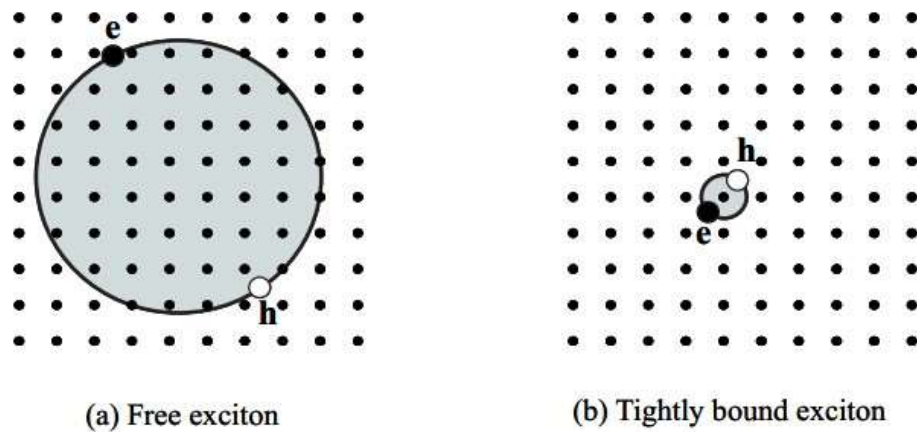


Figure 1.6: Two basic types of excitons. a) Wannier–Mott excitons (free excitons)
b) Frenkel excitons (tightly bound excitons). [17]

Due to large radius (Figure 1.6a) free excitons have smaller binding energies and usually can only be observed at cryogenic temperatures ($k_B T < E_b$). On the other hand, bound excitons possess large binding energies (0.1-1eV) which allows them to survive even at room temperature. In the case of TMDs, these binding energies can reach up to **320 meV for WS₂**, which are several times higher than bulk semiconductors [18]. Figure 1.7 exhibits the result of quantum confinement and reduced dielectric screening in 2D materials, which leads to larger energy gap and exciton binding energies, comparing with the 3D systems.

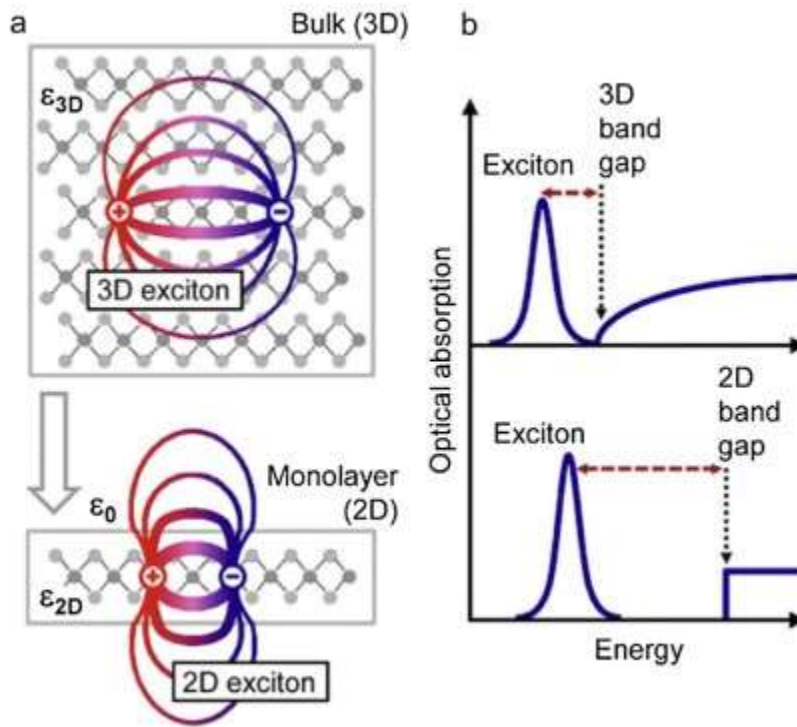


Figure 1.7: Quantum confinement and reduced dielectric screening in 2D materials. a) Confinement of charged carriers due to absence of adjacent layers (smaller exciton radius) b) Increased energy band gap and larger binding energies in 2D systems. [18]

The presence of high binding energies in 2D semiconducting materials led to a distinction between the electronic (E_g) and optical (E_{opt}) band gaps. As Figure 1.8a illustrates, the difference between the electronic and optical band gaps corresponds to the binding energy of the exciton [19]. Finally, Figure 1.8b shows the spin-orbit coupling and the subsequent valence band splitting in TMDs with the generic form WX_2 .

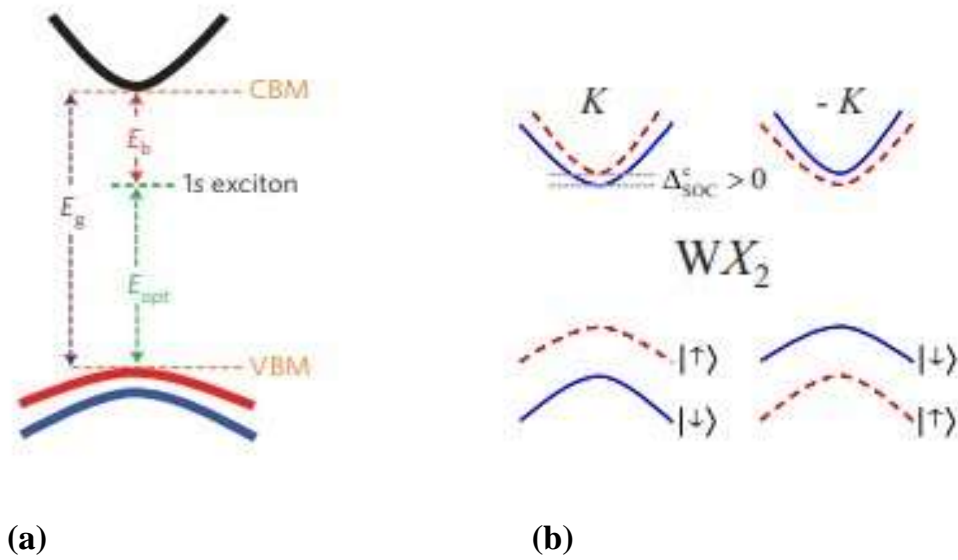


Figure 1.8: a) Energy diagram indicating the electronic bandgap (E_g), the optical bandgap (E_{opt}), and the exciton binding energy (E_b). b) Conduction- and valence- band spin splitting in the $\pm K$ valleys for WX_2 ($X = S, Se$) [20].

2.1 Raman Spectroscopy

Raman Spectroscopy is a widely used technique for a vast variety of applications in material characterization such as sample identification and crystal structure determination. It is considered as one of the most straightforward ways of observing vibrational transitions between molecules, through the absorption of electromagnetic radiation [21].

The basic principle of Raman Spectroscopy is the Raman effect which is a light scattering phenomenon. When a light of frequency ν_I interacts with a sample it can be reflected, absorbed, transmitted or scattered. The frequency ν_s of the scattered light can either remain the same as the initial frequency (*Rayleigh scattering*) or present a frequency shift (*Raman scattering*), so that $\nu_s = \nu_I \pm \nu_{\text{molecular}}$ (Figure 2.1) [22]. The frequency $\nu_{\text{molecular}}$ is an internal frequency of the molecule corresponding to rotational, vibrational and in some cases electronic molecular transitions. [23]

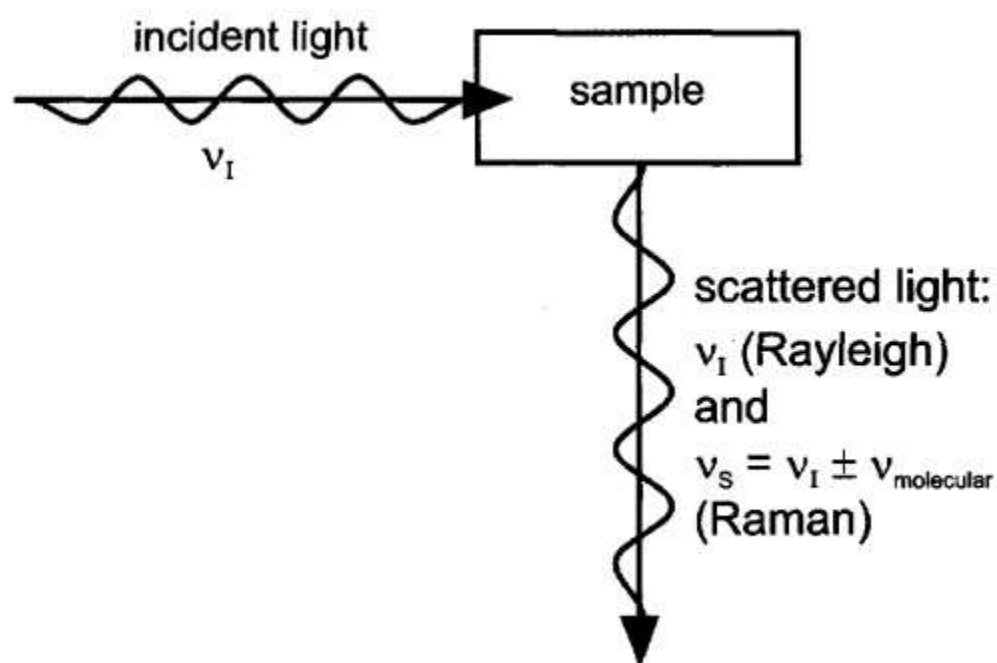


Figure 2.1: Incident light scattered by a sample. [22]

According to the classical model, when an external electric field \mathbf{E} is applied to a molecule a dipole moment is induced. For as long as the applied electric field is not too strong the induced dipole moment μ_{ind} is linearly proportional to the field:

$$\boxed{\mu_{\text{ind}} = \alpha \mathbf{E}} \quad (1)$$

where α is the polarizability of the molecule.

The intensity of the scattered light is proportional to the square of the magnitude of the induced oscillating dipole moment [24]. If any internal motion modulates this oscillating moment, then some other frequencies rise. This results in a static term α_0 and an oscillating sinusoidal term $\alpha_1 \cos(\omega t)$ for polarizability [25]:

$$\boxed{\alpha = \alpha_0 \pm \alpha_1 \cos(\omega t)} \quad (2)$$

where α_1 : amplitude of the sinusoidal term

and $\omega = \omega_{\text{molecular}}$: internal angular frequency

The oscillating electric field of an incident electromagnetic wave (e.g. laser beam) can be written as:

$$\boxed{\mathbf{E} = \mathbf{E}_0 \cos(\omega_I t)} \quad (3)$$

Upon substituting (3) + (2) to (1), we get:

$$\mu_{\text{ind}} = \alpha \mathbf{E} = \alpha \mathbf{E}_0 \cos(\omega_I t)$$

$$\mu_{\text{ind}} = (\alpha_0 + \alpha_1 \cos(\omega t)) \mathbf{E}_0 \cos(\omega_I t)$$

$$= \alpha_0 \mathbf{E}_0 \cos(\omega_I t) + \alpha_1 \mathbf{E}_0 \cos(\omega_I t) \cos(\omega t)$$

$$= \alpha_0 \mathbf{E}_0 \cos(\omega_I t) + [\alpha_1 \mathbf{E}_0 \cos(\omega_I - \omega)t + \alpha_1 \mathbf{E}_0 \cos(\omega_I + \omega)t]/2$$

In the last step the following trigonometric identity was used:

$$\cos\theta\cos\varphi = [\cos(\theta-\varphi) + \cos(\theta+\varphi)]/2$$

This result shows that the oscillating polarizability causes the dipole moment to oscillate at frequencies other than ω_I (where $\omega_I = 2\pi\nu_I$).

$$\mu_{\text{ind}} = \alpha_0 \mathbf{E}_0 \cos(\omega_I t) + [\alpha_1 \mathbf{E}_0 \cos(\omega_I - \omega)t + \alpha_1 \mathbf{E}_0 \cos(\omega_I + \omega)t]/2 \quad (4)$$

By looking at each term of Equation (4) one can see that the first term with the unshifted frequency corresponds to Rayleigh scattering, whereas the lower frequency term ($\omega_I - \omega$) and the higher frequency term ($\omega_I + \omega$) correspond to Stokes and anti-Stokes scattering, respectively [26].

It is noteworthy, that classical interpretation can be misleading, since it predicts that Stokes and anti-Stokes scattering have the same intensity. The energy level diagram (Figure 2.2) proves that anti-Stokes scattering will be weaker because the population in the excited vibrational level is less than that of the ground state [27]. Figure 2.2 illustrates the quantum transitions for all the previous scattering types in agreement with the selection rules.

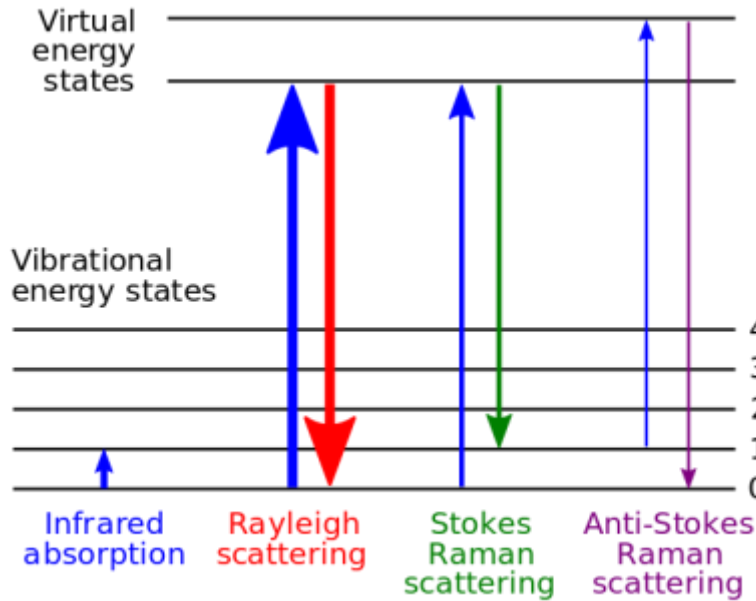


Figure 2.2: Energy diagrams indicating quantum transitions for Rayleigh, Stokes and anti-Stokes scattering. Virtual energy states are not real states of the system [28].

Raman scattering is an extremely weak process as only a small fraction of photon is inelastically scattered. The intensity of Raman peaks is defined by the equation (5) [29]:

$$I = K.\alpha^2.P.\lambda^{-4} \quad (5)$$

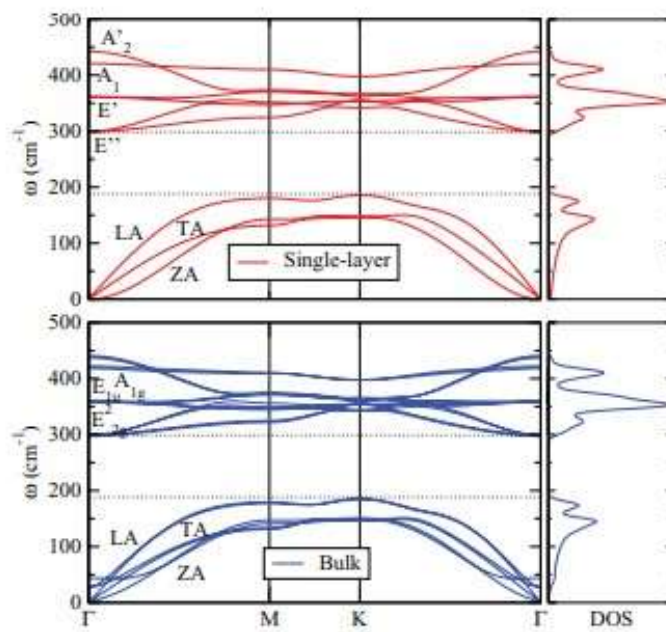
where K is a proportionality constant, α is the polarizability, P is the laser power and λ is the wavelength of incident photons. Therefore, only the laser power and the wavelength can be chosen manually and can be tuned in order to enhance the Raman scattering mechanism. A typical Raman spectrum illustrates the intensity of the scattered light as a function of its frequency or, more commonly, wavenumber difference to the incident radiation. Peaks corresponding to Stokes and Anti-Stokes processes appear symmetrically around the laser line. For this reason, one should study the expected vibrational modes of a sample (sample's fingerprint) beforehand, in order to avoid the overlapping between laser line and Raman modes.

2.2 Phonon Dispersion of monolayer WS₂ and graphene

The phonon dispersion of a crystal corresponds to the relationship between the energies (or frequencies) of the photons as a function of their wave vector and is of fundamental importance in Raman spectroscopy. Figure 2.3a shows the phonon dispersions of single-layer and bulk WS₂, along with the density of states (DOS) [30]. The bulk phonon dispersion has three acoustic modes. Those that vibrate in-plane [longitudinal acoustic (LA) and transverse acoustic (TA)] have a linear dispersion and higher energy than the out-of-plane acoustic (ZA) mode. The latter displays a q^2 dependence analogous to that of the ZA mode in graphene, where q is the phonon wave vector [31].

For the WS₂ monolayer, the difference between the two main vibrational modes A_1 and E' is 60 cm⁻¹ which can be used as a fingerprint in the Raman characterization of WS₂ monolayers [32]. In the single layer, the high frequency Γ modes E_{2g}^1 and E_{1u} collapse into the mode E' . The out-of-plane mode A_{1g} follows the expected trend that the interlayer interaction increases the frequency with respect to the single-layer mode A_1 , because of an additional spring-force between the Sulfur atoms on neighboring layers. In contrast, the E_{2g}^1 mode slightly decreases, due to stronger dielectric screening in bulk WS₂. In both cases the highest peaks in DOS diagrams are located close to the Raman-active modes E_{2g}^1 and A_{1g} (Figure 2.3b).

(a)



(b)

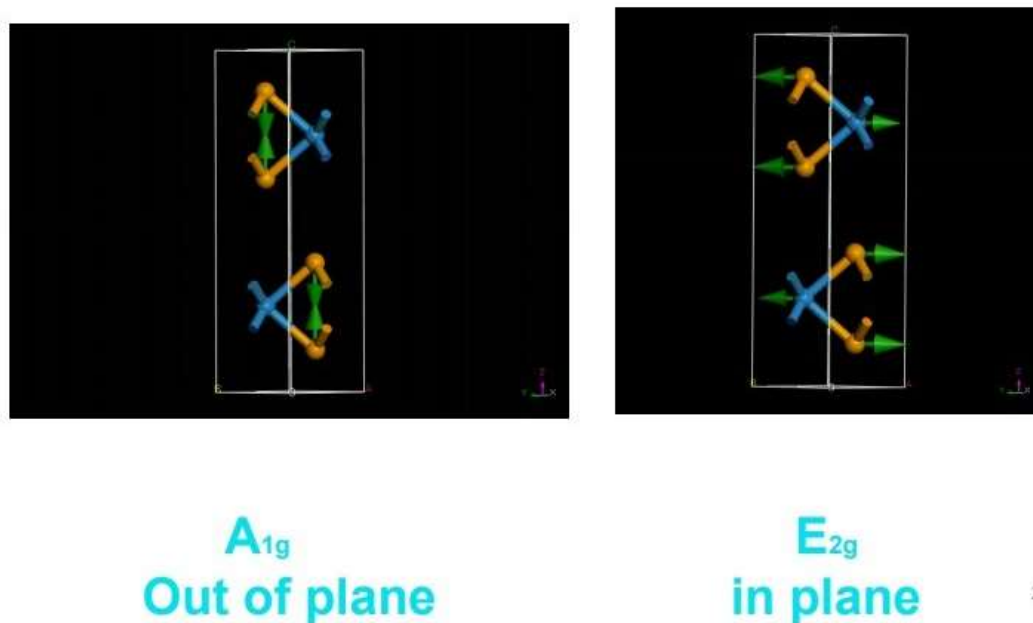


Figure 2.3: a) Phonon dispersion curves and density of states of one-layer and bulk WS₂. b) In-plane phonon mode E_{2g} and out-of-plane mode A_{1g} [33]. Blue spheres correspond to W-atoms whereas orange spheres correspond to sulfur atoms.

For graphene, six phonon dispersion bands, three acoustic (A) and three optic (O) branches exist (Figure 2.4). There are doubly degenerate phonon modes LO and iTO at the Γ point, from which the first order Raman G band arises at approximately 1580 cm^{-1} . This E_{2g} symmetry vibration originates from C–C stretch vibrations in a sp^2 lattice. At the K point, second order processes give rise to the D and G' bands at around 1350 and 2700 cm^{-1} , respectively. The D-band originates from one iTO phonon and a defect phonon, for example, at defects in the lattice or edges. Furthermore, another defect induced band, namely the D' band, is located at around 1620 cm^{-1} . The G' band, although not a first order mode and located at approximately double the frequency of the D-band, is not due to defects, but evolves from two iTO phonons by a double resonance process [34].

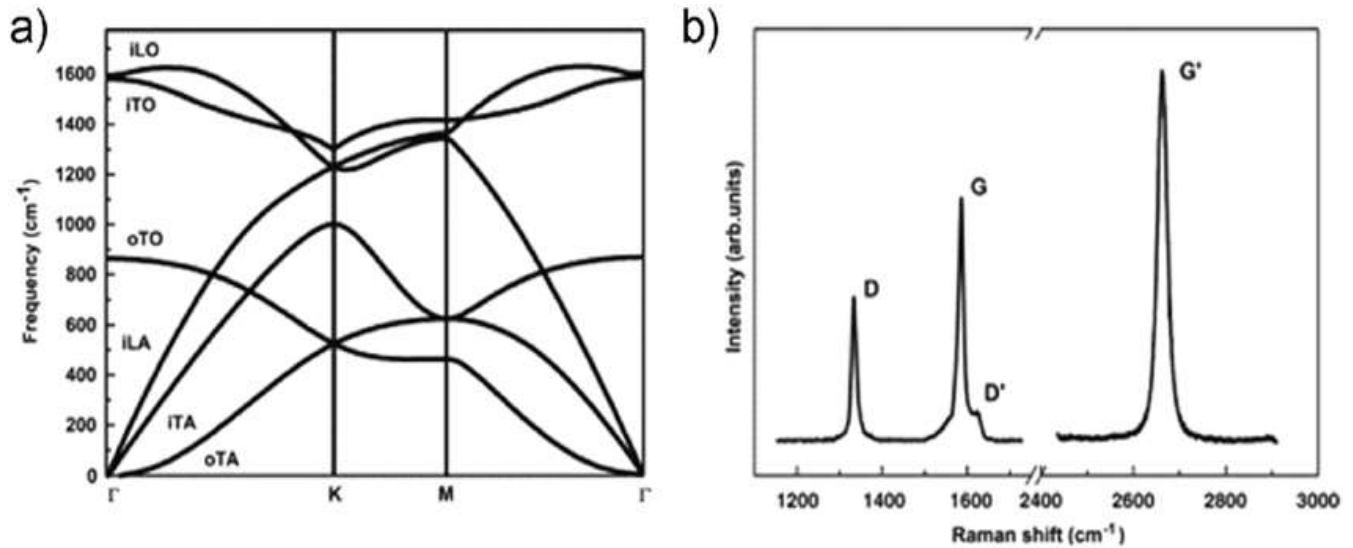


Figure 2.4: a) Calculated phonon dispersion of graphene along the high symmetry points with the path Γ -K-M- Γ . b) Typical Raman spectrum of a graphene edge showing G, G' bands next to defect induced D, D' bands. [34]

2.3 Photoluminescence

Atoms emit light by spontaneous emission when electrons in excited states drop down to a lower energy level by radiative transitions. In solid materials the radiative emission process is called *luminescence*. When the excitation source happens to be a photon, the phenomenon is then called *Photoluminescence*. As Figure 2.5 suggests, a photon is emitted when an electron in an excited state drops down into an empty state in the ground state band. This can happen, only if the lower energy level for the transition is empty, because the Pauli exclusion principle does not allow two electrons to occupy the same quantum state simultaneously [35].

The generation of light is strongly dependent on the energy relaxation processes in the solid. Some relaxation processes can happen without the emission of light, known as non-radiative. For instance, the electron might lose its excitation energy as heat by emitting phonons or transfer the energy to impurities or defects [36]. Therefore, the radiative emission has to compete with the non-radiative process, and one should consider the ratio of radiative time (τ_R) to non-radiative time (τ_{NR}) in order to determine the luminescent efficiency.

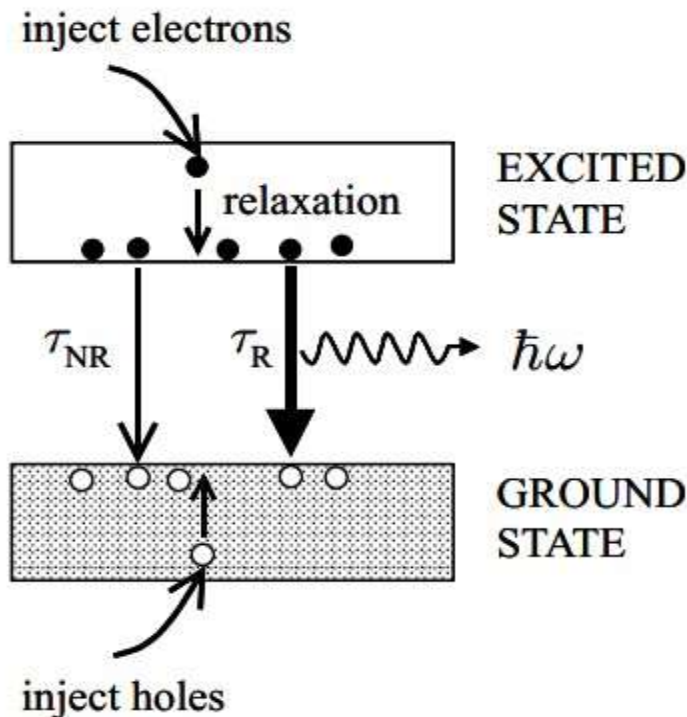


Figure 2.5: Simple scheme of luminescence in a solid. Electrons are injected into the excited state band and relax to the lowest available level before dropping down to empty levels in the ground-state band by emitting a photon. [37]

In the case of a semiconductor, Photoluminescence can occur when photons are absorbed from an excitation source (e.g. laser), and this injects electrons into the conduction band and holes into the valence band. The required condition for this to happen is that the frequency ν_L of the source is chosen so that the energy amount $h\nu_L$ is greater than E_{gap} .

There are very important differences between the optical properties of direct and indirect band gap materials. Therefore, in order to have a better understanding of the excitation and relaxation mechanisms we should consider both the direct and indirect band gap semiconductors. Figure 2.6 presents the band diagrams for an interband luminescence process in a direct and indirect gap semiconductor.

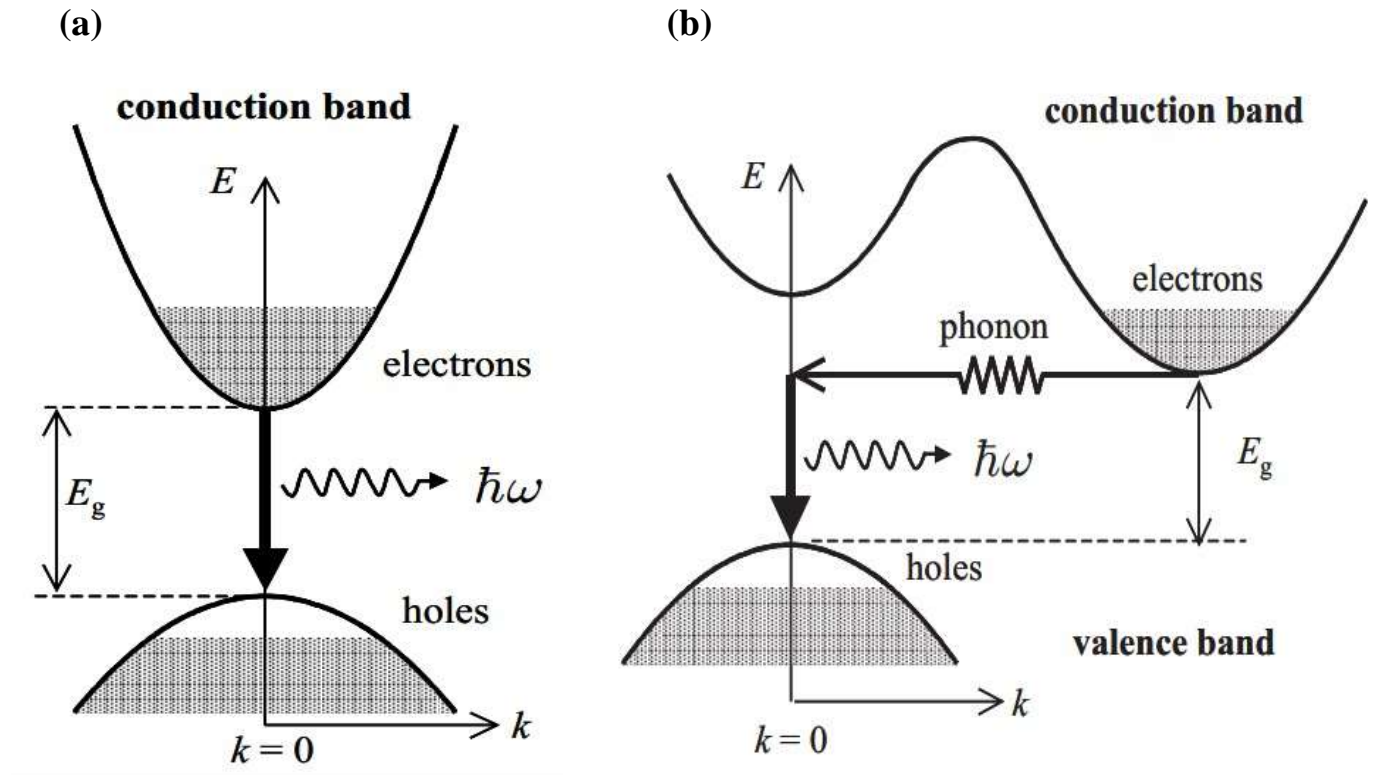


Figure 2.6: Diagram of the interband luminescence process in a) a direct b) an indirect gap semiconductor. The shading indicates that the states are occupied by electrons.[37]

Both Differential Reflectance and Photoluminescence techniques are widely used to determine the number of layers of a 2D sample. Also, they provide information considering the thickness-dependent energy of the different excitonic features, which consequently shows the effect in the band structure of TMDs under changing the number of layers [38].

Differential Reflectance has been recently used to characterize the optical properties of TMDs in a broad range of electromagnetic spectrum (white light). This technique belongs to a broader spectroscopic group called *Absorption Spectroscopy*. The main principle of Absorption Spectroscopy relies on the absorption of electromagnetic radiation, as a function of frequency or wavelength, due to interaction with a sample [39]. Figure 2.7 presents the absorption and emission spectra for an atom and a molecule respectively.

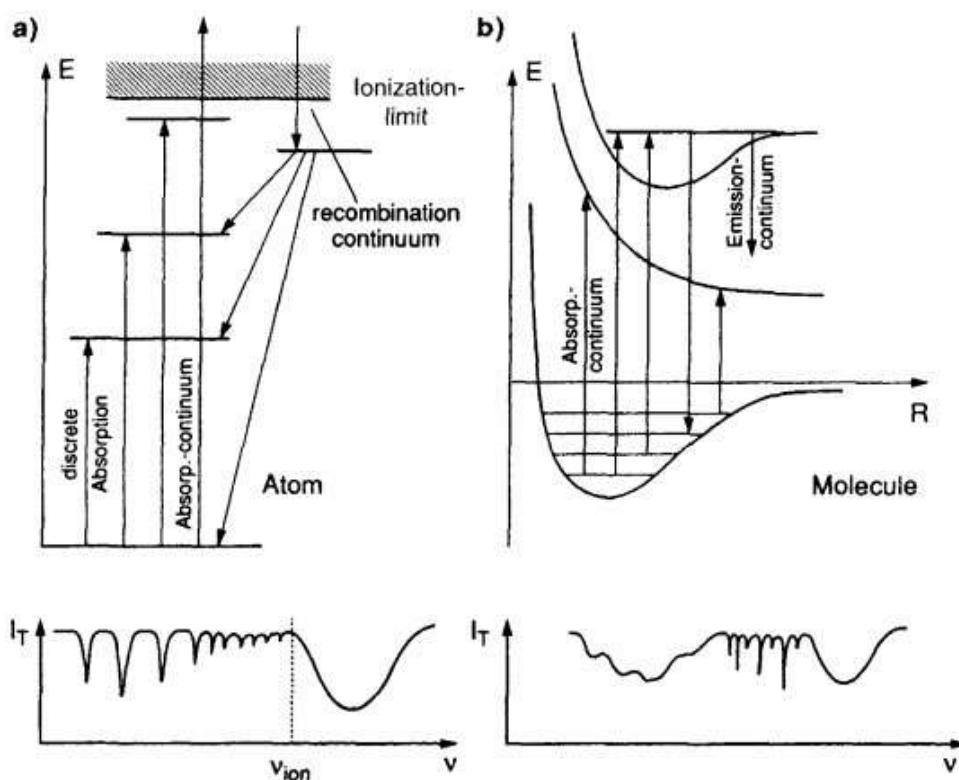


Figure 2.7: Diagram of absorption and emission transitions for a) atoms and b) molecules. The diagrams below illustrate the relation between the intensity and the frequency of the corresponding interband transitions. [27]

Measuring the absorbance of a 2D material (thickness under 1nm) suspended on a transparent substrate is an extremely difficult task to accomplish. Thus, differential reflectance measurements have been introduced in order to study the absorbance of monolayered materials. The fractional change δR is linearly proportional the absorbance coefficient (α) of the material as the following relation suggests [40]:

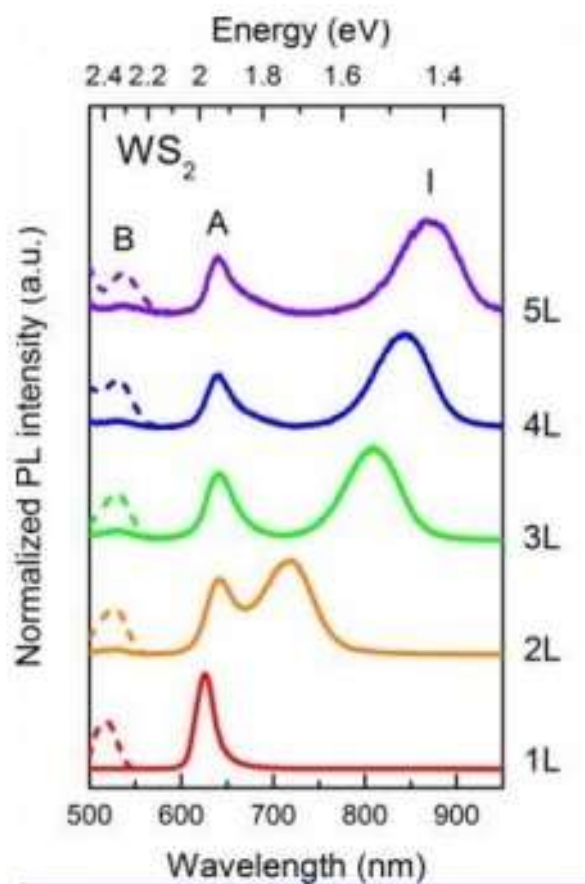
$$(6) \quad \boxed{\frac{R - R_0}{R} = \frac{4n}{n_0^2 - 1} \alpha(\lambda),}$$

where R : The measured reflectance of the material on the substrate.

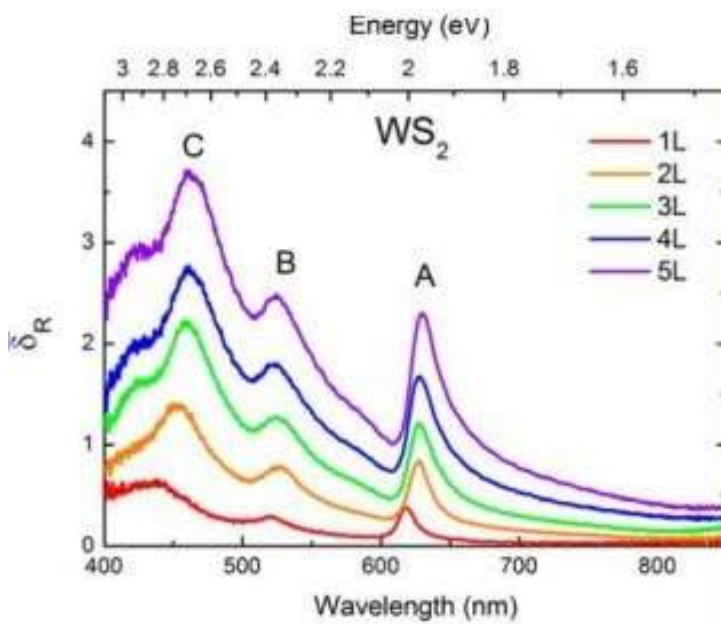
R_0 : The measured reflectance of the substrate.

n, n_0 : The refractive index of the sample and substrate respectively.

According to Zhao et al, Figure 2.8 illustrates the Photoluminescence and Differential Reflectance spectra of 5L-1L WS₂. By looking at Figure 2.8a, all peaks exhibit a gradual but distinct blueshift with decreasing flake thickness. Excitonic absorption peaks A and B which arise from direct gap transitions at the K point are found, respectively, around 625 and 550 nm. Moreover, the energy difference between the A and B peaks, which is an indication of the strength of spin-orbit interaction, is approximately 400 meV. In contrast to absorption, PL spectra show remarkable dependence on flake thickness for both materials as shown in Figure 2.8b. The most notable change is the steep increase in emission intensity when the flake is thinned to a monolayer. Single layer WS₂ exhibits strong emission at the energy corresponding to A excitonic absorption, whereas the emission intensity is dramatically reduced for multilayer flakes.



(a)



(b)

Figure 2.8: a) Normalized PL and b) Differential reflectance spectra of mechanically exfoliated 2H-WS₂ flakes consisting of 1-5 layers. [41]

Part II

Experimental Methods and Results

Experimental Methods

3.1 Optical Setup

The optical setup in Figure 3.1 has been developed at the Ultrafast Laser Micro/Nano Processing Lab (ULMNP) of the Institute of electronic Structure and Laser (IESL) at the Foundation for Research and Technology-Hellas (FORTH). The micro-photoluminescence (μ PL) and the micro-reflectance (μ DR) experiments were carried out with this setup.

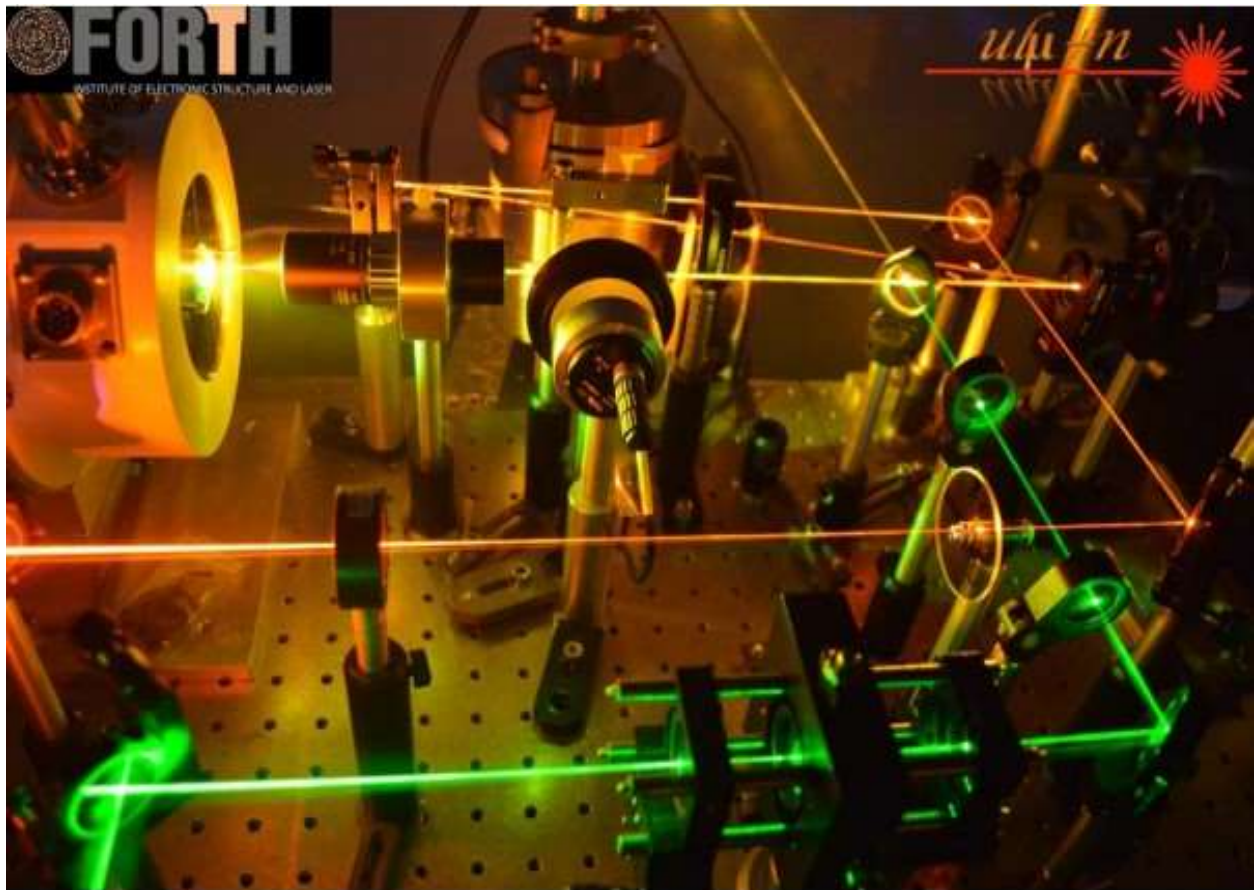


Figure 3.1: Picture of the custom optical setup developed at the ULMNP lab of IESL/FORTH. [42]

An iHR-320 spectrometer (Horiba Scientific/Jobin Yvon Technology) was used in this setup (Figure 3.2a). It is an automated spectrometer with a 320mm focal length (f/4.1 aperture) and offers a 300g/mm grating on its turret: The wavelength accuracy is ± 0.20 nm and the spectral dispersion 2.35nm/mm. The step size of the automated turret is 0.002nm.

The geometry of the monochromator used in the setup is shown in Figure 3.2b. It is a common Czerny–Turner design, where the incoming signal (A) is focused at the entrance slit (B). The slit is placed at the focal point of a parabolic mirror (C) that collimates the divergent incoming light (focused at infinity). The collimated light is then diffracted from a reflective grating (D) and is collected by a second parabolic mirror (E), which refocuses the dispersed light on the exit slit (F). Since the different wavelengths are spread out through the grating, they arrive at a separate point in the exit-slit plane. A rotation of the reflective grating causes the band of wavelengths to move relative to the exit slit, so that the desired entrance slit signal is centered on the exit slit.

A Sincerity multichannel charge-coupled device (CCD) Deep Cooled Camera is attached to the exit of the monochromator. It utilizes the thermoelectric effect to operate at 600C for high signal-to-noise ratio. The CCD sensor contains 1024×256 pixels with a pixel size of 26 μ m×26 μ m. The spectral range is 250nm-1050nm with a quantum efficiency of almost 60% at 750nm.

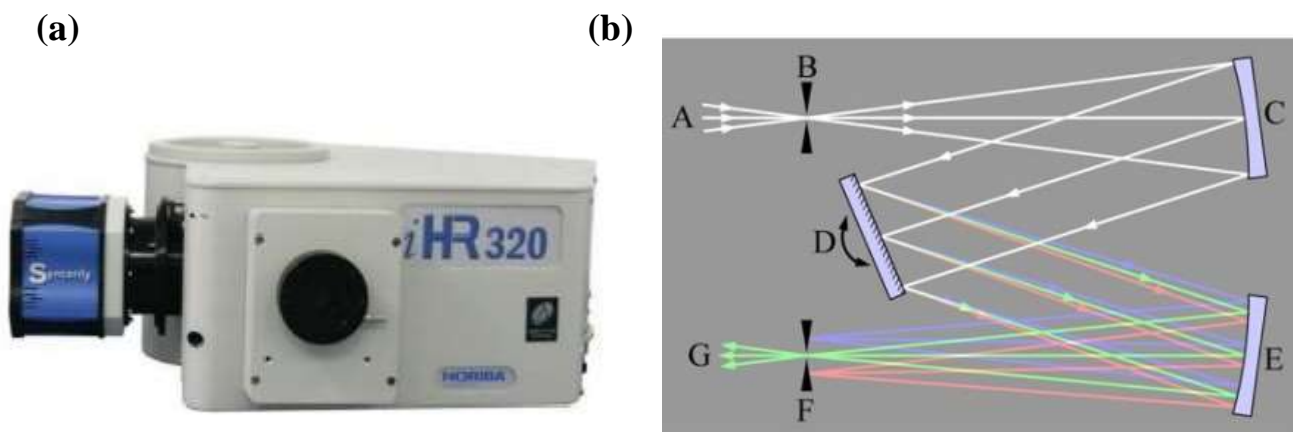


Figure 3.2: a) Picture of the iHR-320 spectrometer. b) Schematic representation of a Czerny Turner monochromator. [42]

3.1.1 micro-PL configuration

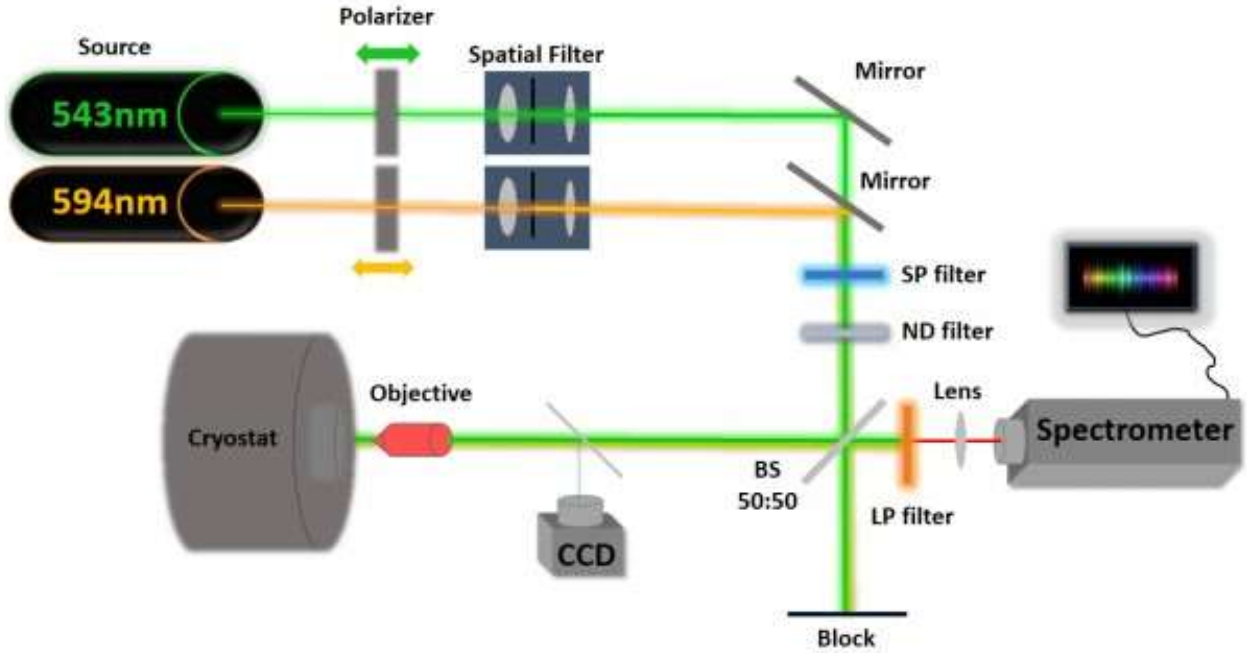


Figure 3.3: Schematic representation of the micro-Photoluminescence (μ PL) configuration. He-Ne 594nm excitation source was not used in this experiment. [42]

Micro-photoluminescence (μ PL) spectra were collected in a backscattering setup shown in Figure 3.3. Experiments were conducted using only the continuous wave (CW) HeNe 543nm excitation source (photon energy: 2.28eV), which is not resonant with the optical gap of monolayer WS_2 . The path of the laser beam is illustrated with green color. At first, the laser beam (s-polarization) passes through a spatial filter (KT310, Thorlabs) for two reasons: the first is to clean the Gaussian beam from its spatially varying intensity noise and acquire a uniform energy distribution. The second is to expand the beam size in order to fit through the aperture of the objective and achieve diffraction limited spot size. After the spatial filter, the beam passes through a short pass (SP) filter (FESH550, Thorlabs) to reduce the noise at higher wavelengths. The power of the laser beam is controlled via a neutral density (ND) filter (0-2 OD, NE520B-A, Thorlabs). A 50:50 beam splitter (BS 50:50, BSW10, Thorlabs) is used to reflect and drive the beam to the objective lens. A Mitutoyo 50x (NA:0.42, $f=200\text{mm}$) focuses down to $\sim 1\mu\text{m}$ the spot size for the sample excitation which is placed inside a cryostat (ST500, Jannis). The position of the sample is controlled with a XYZ mechanical translation stage (PT3, Thorlabs) and the excitation procedure is continuously monitored and controlled via a CCD optical setup.

Following the excitation, the emitted PL signal passes through a long pass (LP) filter (FELH550, Thorlabs) to block the emission of the laser.

3.1.2 micro-R configuration

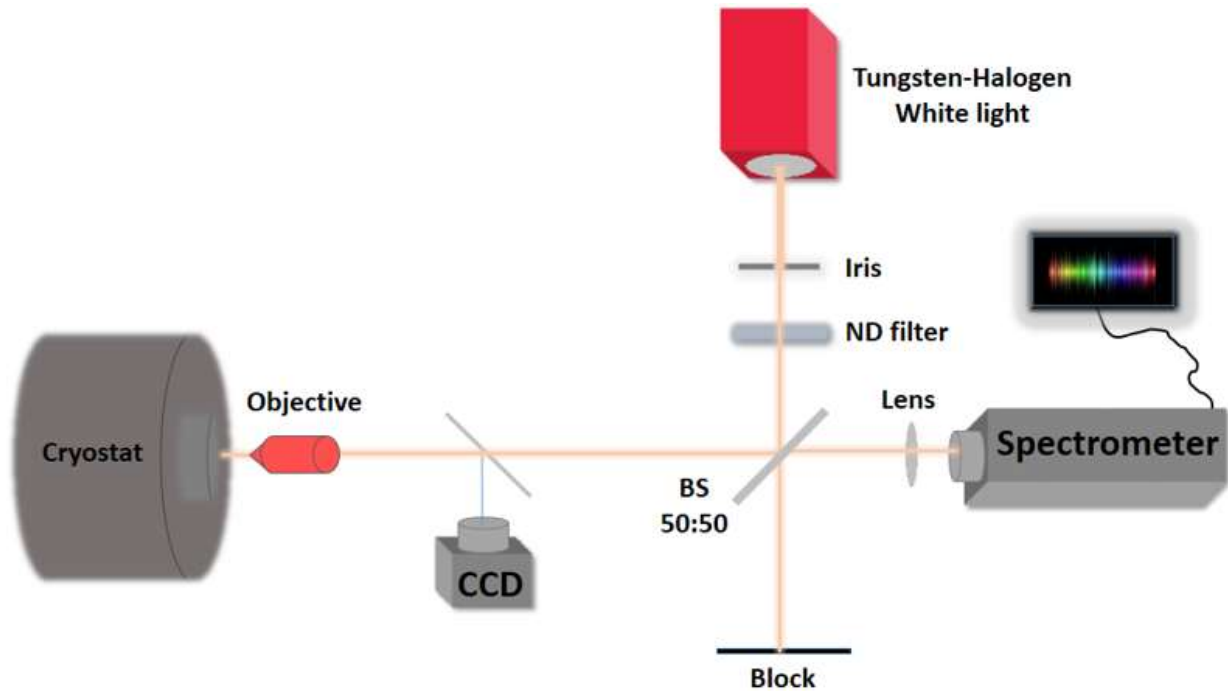


Figure 3.4: Schematic representation of the micro-Differential Reflectance (μ DR) configuration. [42]

The same optical setup can be easily modified by flipping the mirrors of the μ PL configuration and permit the aligned super continuum light (360nm - 2600nm) of a stabilized tungsten-halogen source (SL201L, Thorlabs) to pass through an iris and follow the same optical path as discussed in section 3.1.1. It is apparent that in order to perform a differential reflectance experiment in the same optical path, the long and short pass filters must be first removed in order to exploit the spectrum of the super continuum light efficiently (Figure 3.4). The diameter of the white light spot size on the sample is approximately $3\mu\text{m}$.

In a typical experiment, the electronic transitions of a very thin film (for example TMD monolayers) are probed with the broad-band light and the reflected signal that follows the backscattering geometry is measured. However, since the flakes are atomically thin and placed on SiO₂/Si substrate, the reflected light spectra include the illumination source profile and the sample's transmission and absorption. They also include the substrate's reflection and absorption, and resonant effects due to the thickness of the SiO₂. To distinguish the contribution from the monolayer TMD flake, we take the difference between the intensity measured from the flake, R , from the substrate (just off the flake), R_{sub} , and normalize to the intensity from the flake, $DR = \frac{R - R_{\text{sub}}}{R}$.

3.2 Cryogenic System

The importance of incorporating a cryogenic system in our experiments should be highlighted. At elevated temperatures, thermal effects caused by carrier-phonon scattering play a significant role. Such mechanisms could hide information about excitonic transitions when performing Photoluminescence measurements. The cryogenic system used in the temperature dependent-PL experiment that is described in Section 4.4, is shown in Figure 3.5.

The cryogenic system consists of 6 main parts: the LHe cryostat (ST500, Janis), the transfer line (Standard Flexible Liquid Helium Transfer Line, Janis), a liquid nitrogen 20lt storage dewar (Janis), the temperature controller (Model 335, Lake Shore Cryotronics) a mechanical pump and a turbo pump. The cryostat is a continuous flow research cryostat that performs in the temperature range from 3.5K to 475K (Figure 3.5a). Liquid helium (LHe) or nitrogen (LN) is continuously transferred through a high efficiency super insulated line to a copper sample mount inside the cryostat vacuum jacket. A needle valve is incorporated in the transfer line and is used to regulate the flow of cryogens to the sample mount (Figure 3.5b). Inside the transfer line is a length of flexible metal tubing surrounded by multiple radiation shields and vacuum insulation.

Specially constructed spacers prevent the inner line from contacting the outer vacuum jacket for maximum efficiency during operation. One end of the transfer line is inserted into the cryogen storage dewar, while the other end is inserted into the cryostat. The liquid helium and nitrogen dewars consist of one or more reservoirs, surrounded by a vacuum jacket, which isolates these reservoirs from room temperatures. For proper performance of the cooling procedure, the system must be evacuated to remove all the air and the outgassing from the bellows and other parts of the cryostat. Better vacuum levels

provide greater insulation, resulting in shorter cooldown times and lower temperatures in the sample mount.

In our cryogenic system, a combination of a mechanical pump with a turbo pump evacuate the chamber of the cryostat to a pressure of 10^{-5} Torr which is sufficient for LHe and LN measurements. The temperature of the samples is controlled with a two-channel temperature controller with configurable heater outputs delivering a total of 75W of low noise heater power.

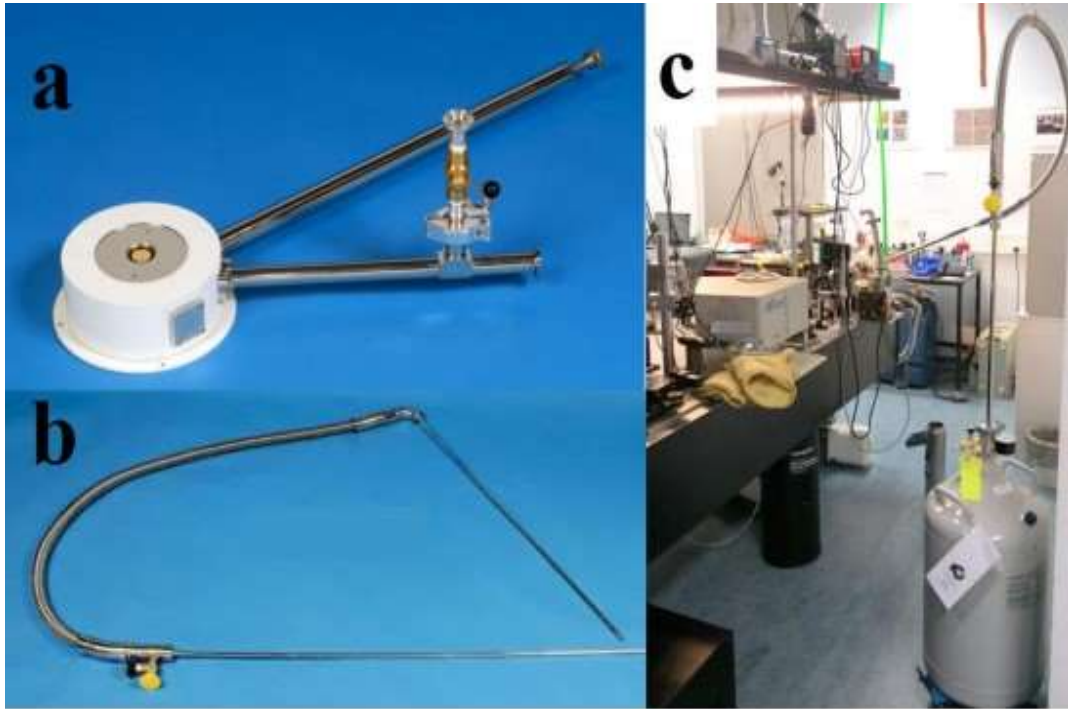


Figure 3.5: a) ST500 cryostat. b) Standard flexible liquid helium transfer line. c) Cryogenic system at the ULMNP lab. [42]

3.3 Sample preparation

The correct observation and thickness identification of 2D materials has been a difficult task so far. For this reason, the right substrate with the optimum thickness plays a crucial role. It has been reported that Si/SiO₂ substrate provides the best optical contrast, while the optimum values considering the thickness of Si/SiO₂ are 90 and 285nm [43]. WS₂ and graphene flakes used in our experiments (Section 4.1), were mechanically exfoliated from a bulk crystal using a Scotch tape and subsequently deposited on 290nm Si/SiO₂ wafers. The adhesive-tape (or Scotch tape) based mechanical exfoliation process is reported to be the best process for producing high quality graphene sheets but suffers from low yield and small size of sheets (~ ten to hundred microns square) (Novoselov et al., 2012) [44].

Mechanical exfoliation procedure is described in the following steps. At first, we isolated a small portion of WS₂ bulk crystal. Then, we used a diamond knife to cut a ~1cm x 1cm piece of Si/SiO₂ which will be used as our substrate. Next, we obtained a typical Scotch tape folded on the two sides as Figure 3.6 shows.

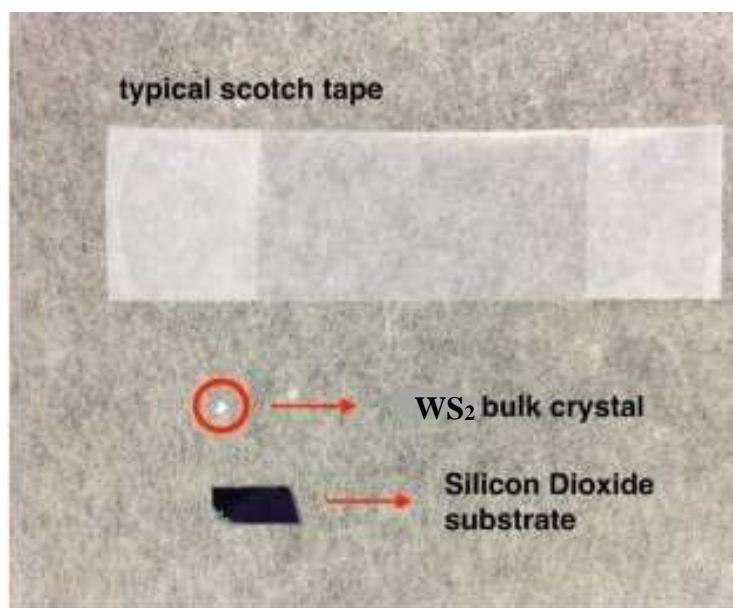


Figure 3.6: Small piece of WS₂ bulk crystal, Si/SiO₂ substrate and a typical Scotch tape used in Mechanical exfoliation procedure. [45]

The second step is to place the bulk WS_2 on the sticky side of the tape and carry out a repetitive folding-unfolding process, by which the bulk sample is spreading along the tape (Figure 3.7).

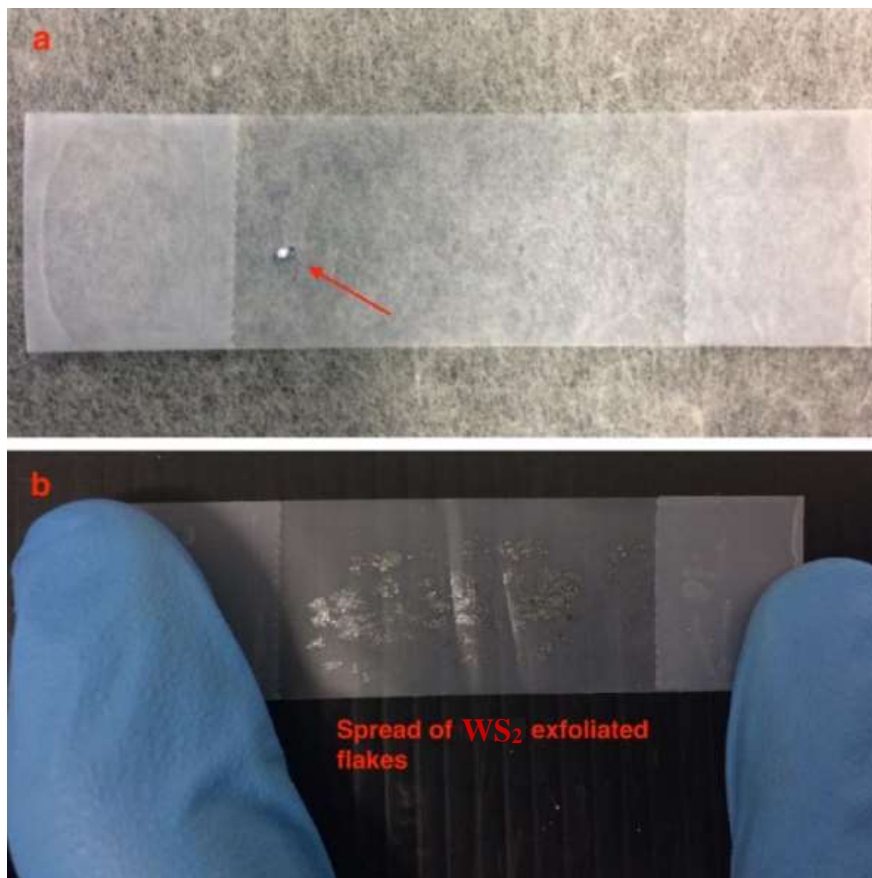


Figure 3.7: a) Bulk WS_2 flake placed on the sticky side of scotch-tape. b) Spread of WS_2 flakes. [45]

Subsequently, we isolate a small area of PDMS (polydimethylsiloxane) on a glass-slide. The PDMS material was fabricated with certain concentration and elasticity in order to facilitate the release of the monolayer. Afterwards, we transfer the exfoliated WS_2 flakes directly from the Scotch tape to the PDMS surface. It is reported in several papers, that the use of PMDS is by far the easiest and fastest exfoliation method [46]. In Figure 3.8 we present an attempt for quantitative comparison between different deterministic placement methods, reported by Frisenda et al. The last step is to realize the monolayer under the optical microscope (Figure 3.9). In case we cannot find a single layer flake, we repeatedly use the Scotch tape to remove WS_2 layers in order to reduce the thickness of our sample.

Method	Cleanness	Easiness	Speed	Notes
PMMA carrier layer	***	***	***	Spin-coating is needed, direct contact with polymer.
Elvacite sacrificial layer	*	***	***	Capillary forces, spin-coating is needed, direct contact with polymer.
Wedging	*	**	***	Capillary forces, dip-coating is needed, difficult alignment, direct contact with polymer, transfer over curved or uneven surfaces is possible.
PDMS dry transfer	***	*****	*****	Direct contact with polymer.
Van der Waals pick-up	*****	*	**	Spin-coating is needed, several steps involved, only works to transfer heterostructures, direct contact with the polymer only for the topmost layer.

Figure 3.8: Table presenting a qualitative comparison in terms of cleanness, easiness and speed between different deterministic placement methods. [46]

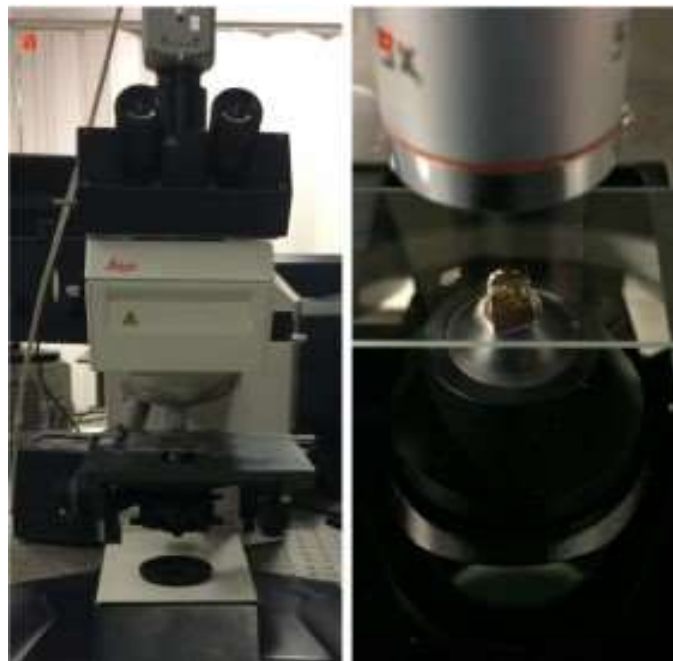
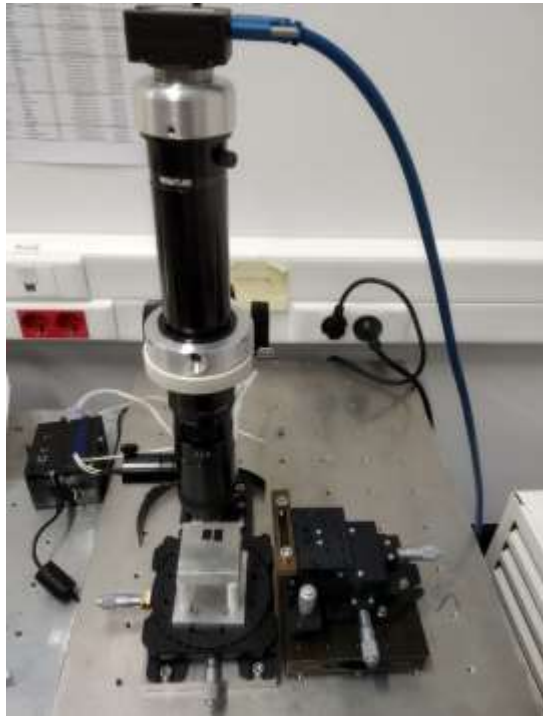


Figure 3.9: a) Leica optical microscope used to investigate the samples. b) Substrate placement under the microscope. [45]

The same procedure was carried out for the exfoliation of a few-layered graphene sample. Unlike WS₂ we were not in need of a single graphene layer for the fabrication of the heterostructure samples. The identification of the single layer WS₂ and few layered graphene was completed after the samples were examined under Raman characterization at room temperature. Particularly, if the energy difference between the two main vibrational modes E' and A1' of a single WS₂ layer is equal to 59–61cm⁻¹, then the existence of the single layer limit was confirmed [47]. To further confirm the existence of monolayers, a combination of photoluminescence (PL) and differential reflectance studies was employed.

The heterostructure fabrication procedure was performed using the deterministic transfer setup shown in Figure 3.10.

(a)



(b)

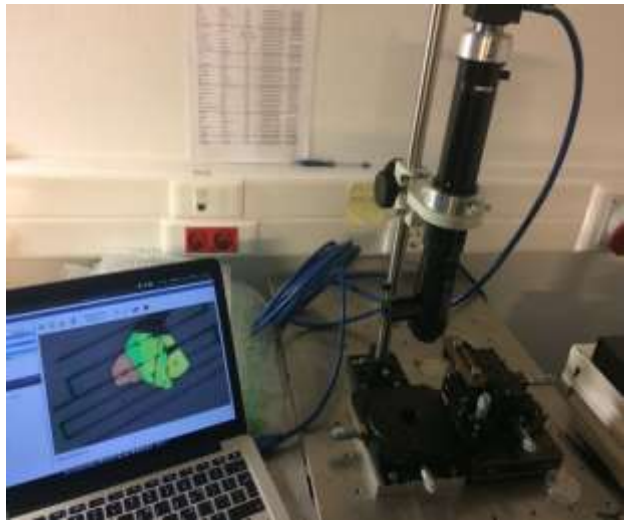


Figure 3.10: a) Picture of the deterministic transfer setup in our lab. The sample under examination is placed on the hot plate. b) The coupling of the heterostructure layers can be monitored.

Every WS₂/graphene heterostructure was fabricated following the next steps. Starting with, we place the substrate/graphene on top of a hot place/base using a carbon tape for stability. The hot place is controlled through a XYΘ micromechanical stage. Then, we set the temperature of the hot plate to 60°C and mount the glass-slide with the heterostructure sample on the XYZ micromechanical stage. When the hot plate reaches the right temperature, we align the sample with the substrate/graphene in order to proceed with the stamping. Keeping the hot plate around 60°C is critical, because PDMS exhibits smooth release which is characteristic of the material [48]. Furthermore, we observe and control the alignment between few layer-graphene and WS₂ flakes through the microscope which is connected to our laptop. This can be done due to the transparency of the glass-slide. After the coupling of the layers we increase the temperature to 150°C to follow the annealing treatment, as discussed in Section 4.3.

3.3.1 Sample definition

In this section, we will define the heterostructure samples that were under examination. Our reference sample with the following configuration **Si_SiO₂/WS₂** will be mentioned as sample **A**. Sample **B** stands for **Si_SiO₂/graphene/WS₂** heterostructure, whereas the sandwiched configuration **Si_SiO₂/graphene/WS₂/graphene** will be referred as Sample **C**. Section 4 will be entirely based on the previous sample definition.

Experimental Results and Discussion

4.1 Spectroscopic study of samples

First and foremost, we isolated and identified a single WS₂ layer using an optical microscope. The obtained optical image in Figure 4.1a indicates the monolayer area, which can be distinguished from the optical contrast compared to the bulk material. As discussed in Section 3.3, a 285 nm thickness Si/SiO₂ substrate provides the optimal contrast for the optical investigation of monolayers. The next step is the characterization of the WS₂ monolayer through Raman spectroscopy. Figure 4.1b shows two prominent vibrational modes of WS₂, which correspond to E' (in plane) and A₁' (out of plane) vibrations, having an energy difference of $\sim 60 \text{ cm}^{-1}$. The aforementioned energy difference is characteristic of the material and confirms the existence of monolayer WS₂. The sharp peak at 521 cm^{-1} corresponds to the main LO and TO (degenerate) vibrational modes of Si atoms of the substrate at the Γ -point of the Brillouin zone. The lateral dimensions of the sample are approximately $10 \mu\text{m}$.

Identification and characterization of sample A

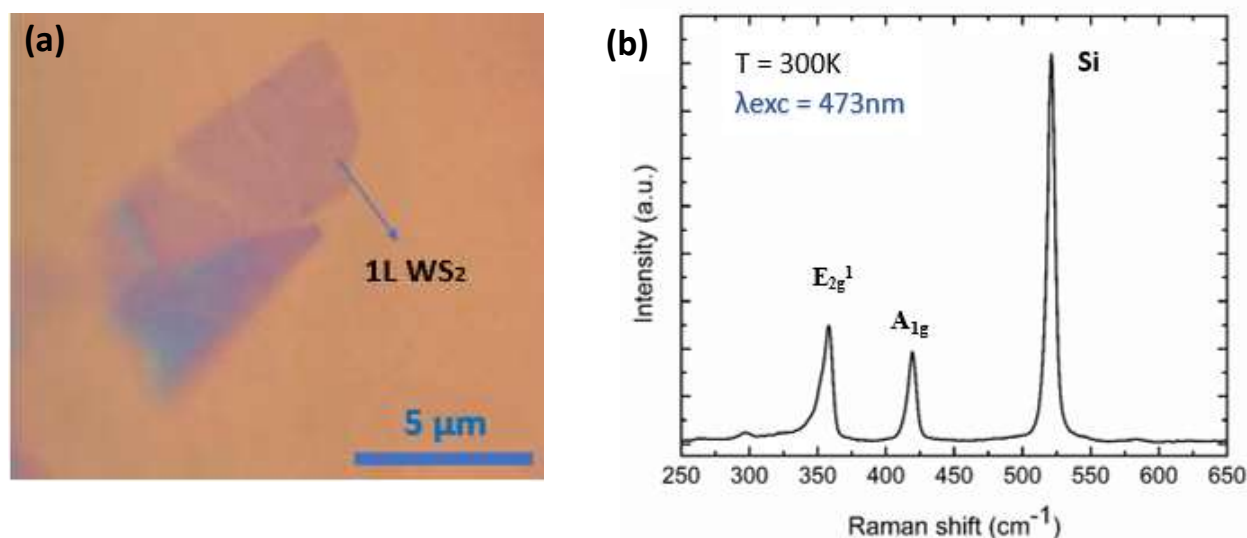


Figure 4.1: a) Optical microscope image of a monolayer WS₂. b) Raman Spectrum of sample A at room temperature.

A standard spectroscopic set of techniques was further applied. We wanted to examine the behavior of sample A under Photoluminescence (PL) and Differential Reflectance (DR) studies. This is an important step, because sample A was used as our reference sample which provided a platform for comparison between the other two samples. Figure 4.2 illustrates PL and DR spectra of Sample A which were conducted at room temperature. A prominent peak at 2.02 eV corresponds to the energy of neutral exciton (A exciton) (Figure 4.2a). According to literature, a much weaker peak was expected at lower energy, indicating the existence of a trion (charged exciton) [49]. We suspect that the absence of charged exciton peak in our PL spectrum is due to inadequate excitation power which would probe the generation of such quasi-particles in our system. Furthermore, the results from DR experiment agree with the previous PL findings in respect to the position of A exciton. Additionally, Figure 4.2b revealed the existence of another exciton (B exciton) at larger energy (~ 2.4 eV) comparing to the A exciton. It is noteworthy, that PL and DR findings could be used as supplemental information to Raman spectroscopy in order to complete the characterization of the sample.

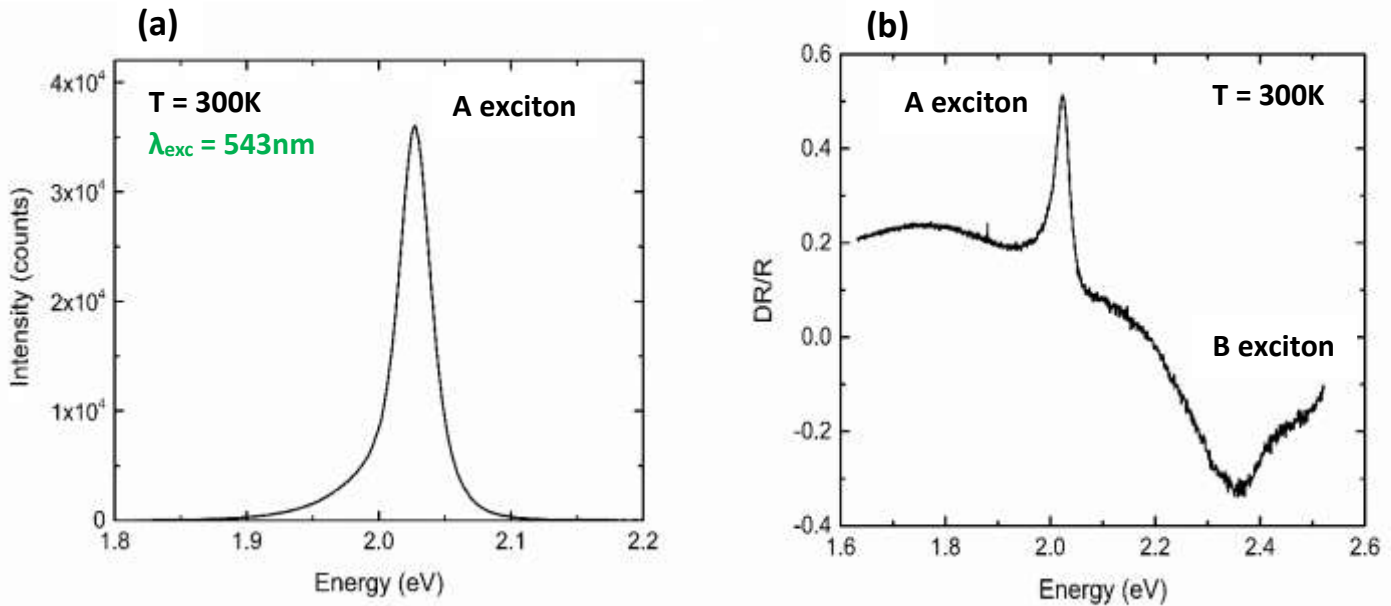


Figure 4.2: a) Photoluminescence and b) Differential Reflectance of sample A at room temperature.

The same procedure was followed for the identification and characterization of Sample B. Figure 4.3 shows two different areas under examination, with the position of the laser spot varying from close to the edge of the for monolayer (Figure 4.3a) to the center of it (Figure 4.3b). In contrast to sample A, the Raman spectrum of sample B exhibited two additional sharp peaks at $\sim 1580\text{ cm}^{-1}$ and $\sim 2700\text{ cm}^{-1}$ which correspond to G and G' (2D) graphene bands, respectively (Figure 4.3c). As mentioned in Section 2.2, the first order Raman G band originates from C–C stretch vibrations in a sp^2 lattice, whereas the G' band evolves from two iTO phonons by a double resonance process.

Identification and characterization of sample B

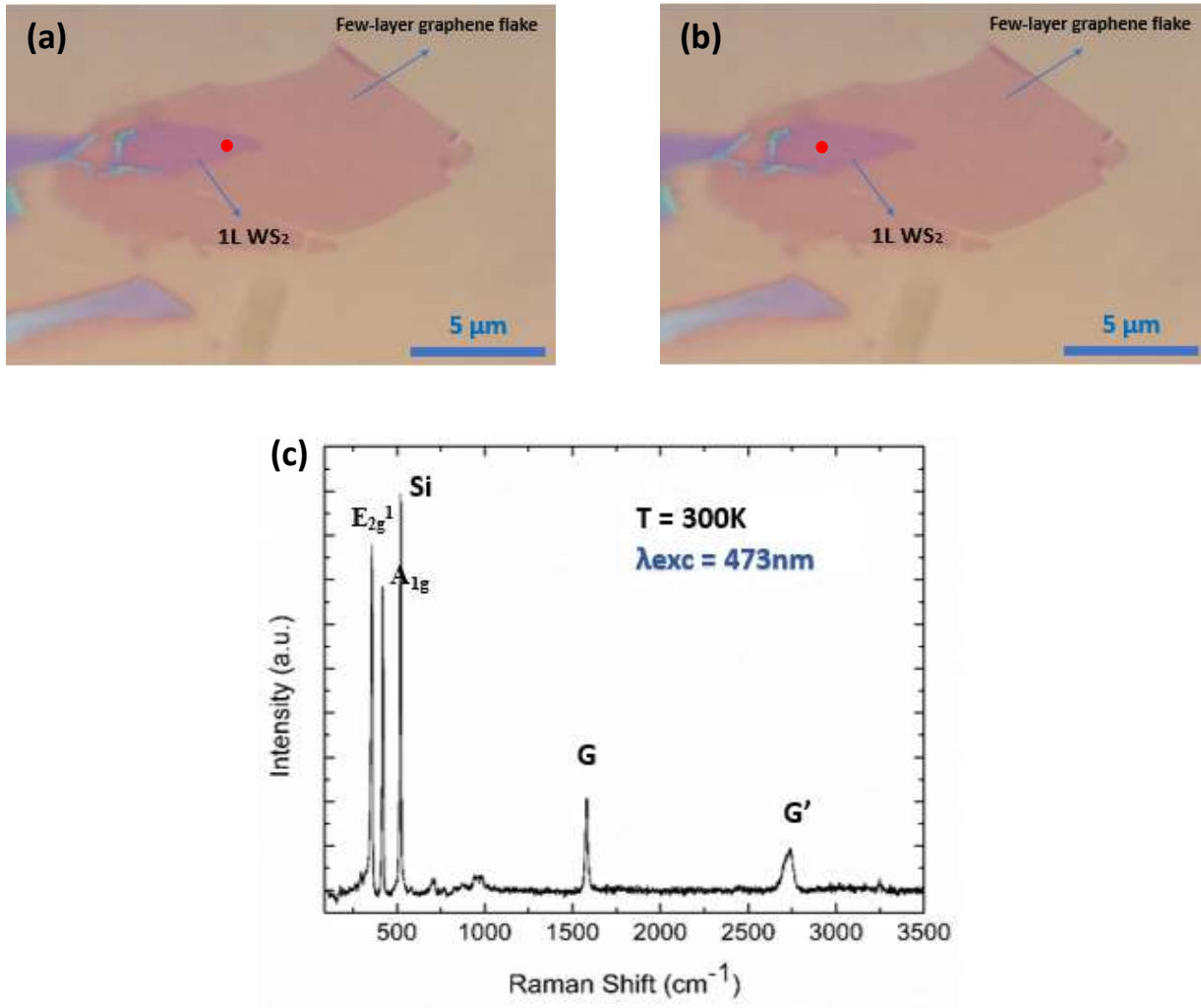


Figure 4.3: Optical microscope image of sample B indicating a laser target a) closer to tip and b) center of monolayer WS₂. c) Raman Spectrum of sample B at room temperature.

At this point, we only used mechanical exfoliation and dry-transfer methods for fabricating our heterostructure samples. Thus, the coupling between adjacent layers was under examination. We further proceeded with a Photoluminescence experiment, acquiring information from different areas of sample B in order to evaluate the coupling. The laser targets of Figure 4.3a, 4.3b correspond to the PL spectra presented in Figure 4.4. In Figure 4.4a, there is a small red shift of the peak alongside with a slight bending of the overall spectral line shape. An even more unexpected behavior is shown in Figure 4.4b, where a weak second peak rises at around 1.93 eV. Overall, it was apparent from both diagrams that there was a lack of consistency in the results corresponding to neighboring areas of sample B and the coupling between layers was under question. Therefore, a further DR examination of the sample was not required due to the confirmation of insufficient coupling based on our current findings.

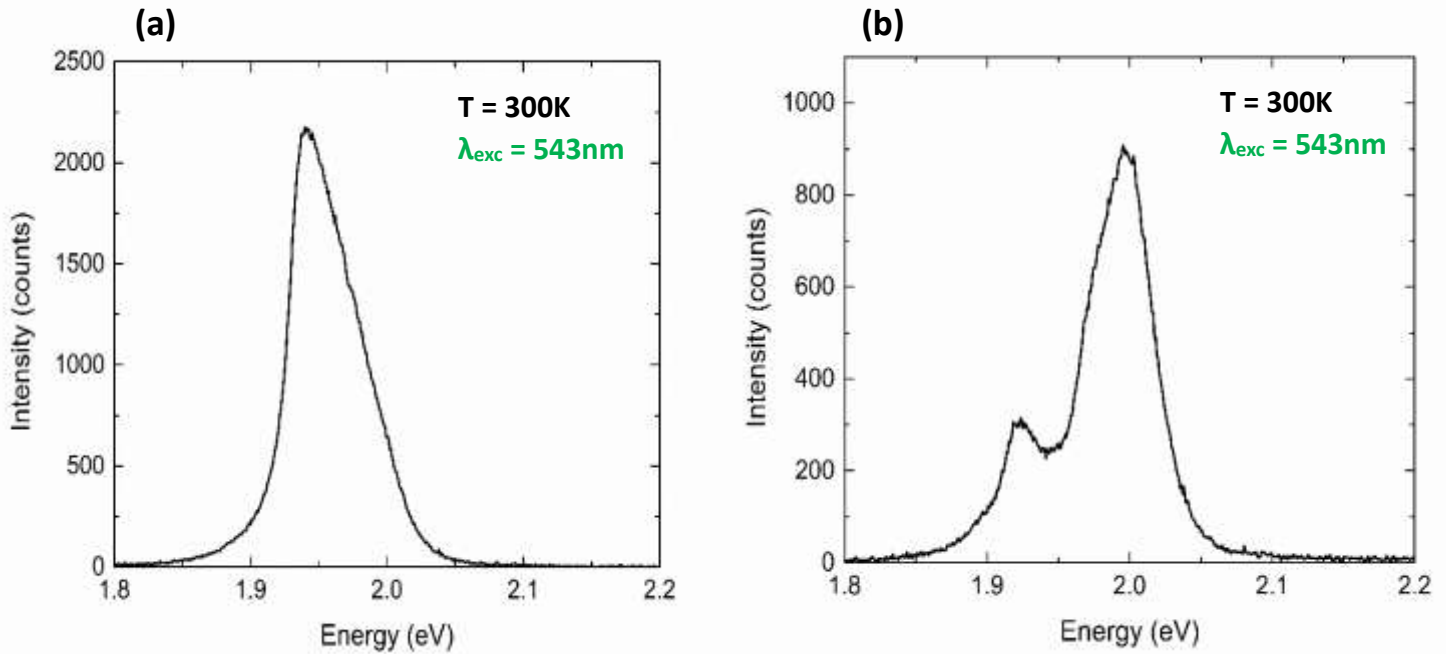


Figure 4.4: Photoluminescence of sample B at room temperature for laser targets of a) Figure 4.3a and b) 4.3b.

Sample C was our last sample under examination and the most challenging one in respect to its fabrication. In addition, the identification of such a sandwiched heterostructure was not a standard process. Figure 4.5a depicts the optical microscope image of sample C with a dispersion of blue marks spread along the sample. During the dry-transfer procedure of fabricating the sample, impurities were trapped between the layers which also affected the heterostructure's coupling. The results of Raman spectroscopy (Figure 4.5b) are in general agreement with the vibrational modes depicted in the previous Raman spectrum of sample B.

Identification and characterization of sample C

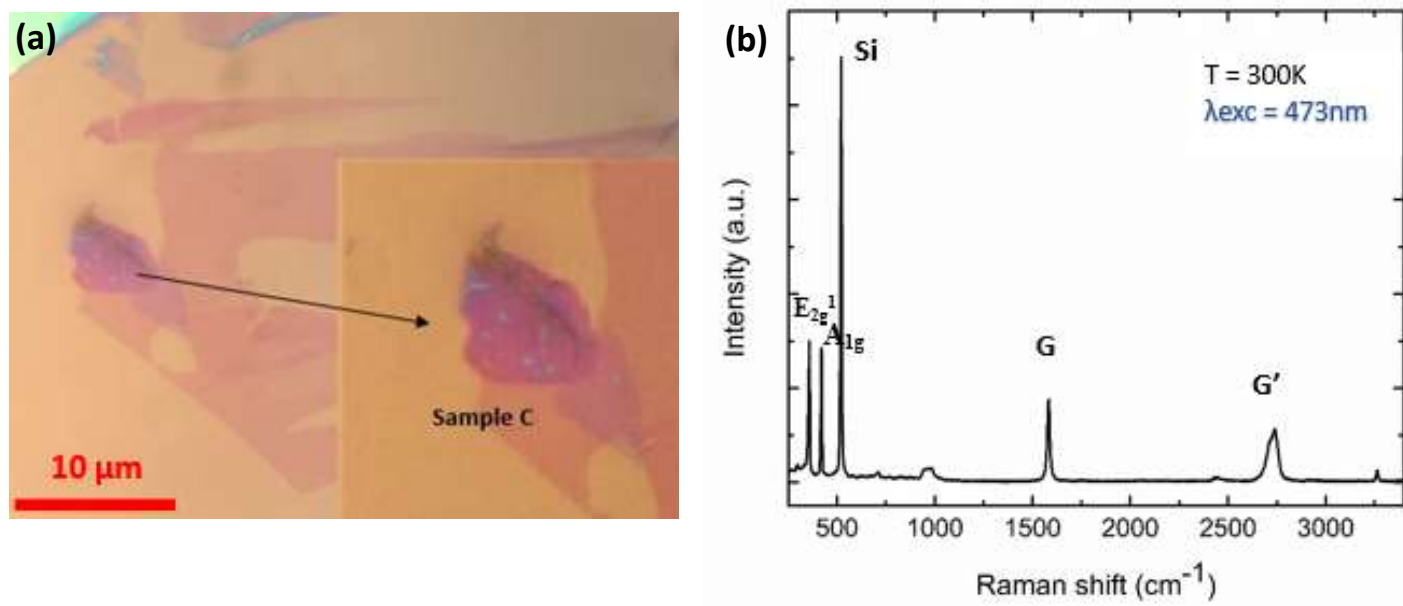


Figure 4.5: a) Optical microscope image of sample C. b) Raman spectrum of sample C at room temperature.

Additional information was gained after conducting Photoluminescence and Differential Reflectance experiments, at room temperature. Particularly, PL of sample C (Figure 4.6a) presented a larger red shift, with the exciton peak located at around 1.96 eV. Moreover, there is an asymmetry on both sides of the peak at the energy range of 1.85 eV-1.95 eV. Thus, the line shape of PL suggests hidden features [50]. An important comparison between PL spectra of sample A (Figure 4.2a), sample B (Figure 4.4) and sample C (Figure 4.6a) has to be made. There is a significant decrease of PL intensity, known as “quenching”, observed from comparing samples A-C. According to literature, “quenching” of PL intensity is indicative of a heterostructure’s coupling [51]. Results in DR data confirmed the existence of A exciton at 1.96 eV but did not yield valuable information about B exciton (Figure 4.6b). Overall, the yielded substrate reflectance presented uncommon behavior. By looking at the energy range of 1.6 eV-1.9 eV one can observe a sharp rise, while the emerging peak at approximately 2.1 eV is due to the white light lamp. Based on our current results, further investigation on the fabrication and coupling methods for our WS₂/graphene heterostructure samples had to be done.

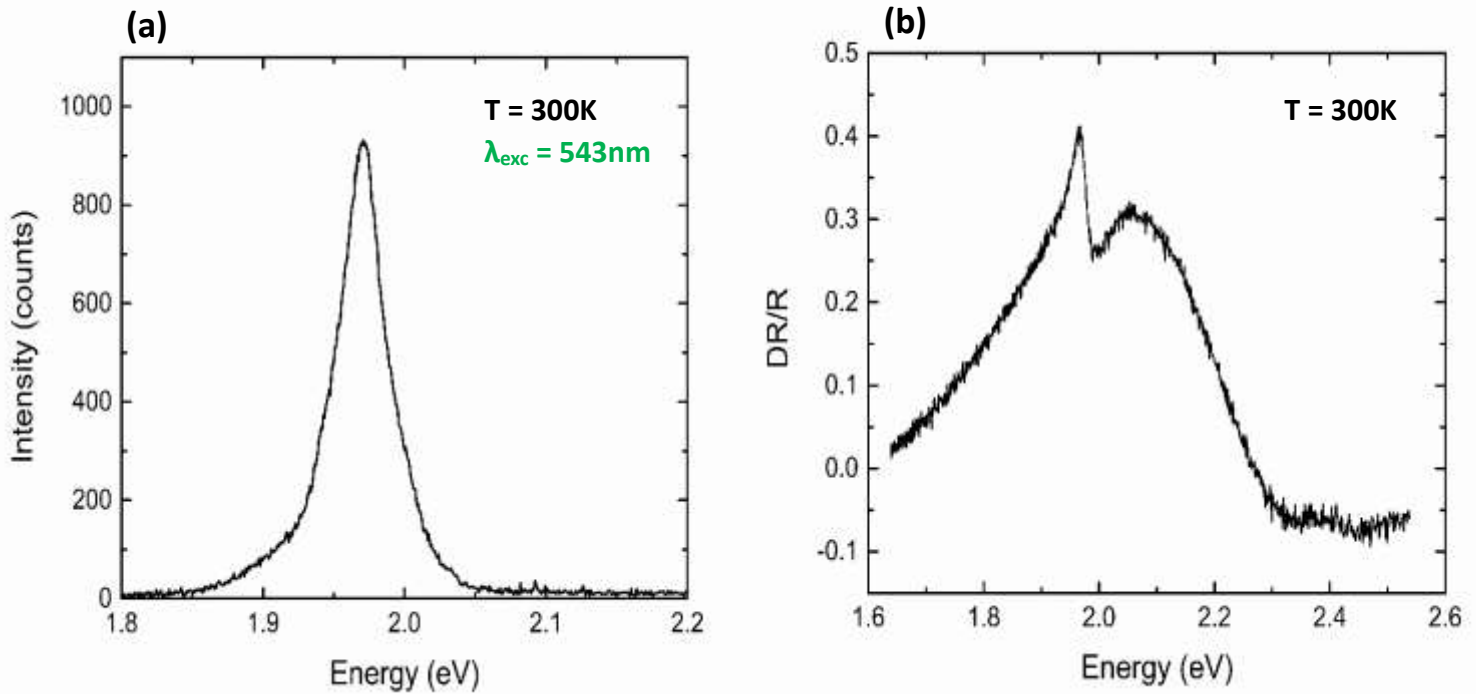


Figure 4.6: (a) Photoluminescence and (b) Differential Reflectance of sample C at room temperature.

4.2 Annealing procedure

Sample Fabrication Steps:

1. Sonication Bath Protocol

(cleaning the substrate prior to transferring any material on)

- 20min in acetone
- 20min in ethanol
- 20min in distilled water

2. Blow-drying the substrate with N₂ gas

3. 30min thermal treatment of the substrate at 150°C (1st time)

4. Mechanical exfoliation of few-layer Graphene on the substrate

5. 30min thermal treatment of the substrate containing few-layer Graphene (Si/SiO₂_Graphene) at 150°C (2nd time)

6. Mechanical exfoliation of bulk WS₂ crystal directly on PDMS in order to create monolayer of WS₂

7. Identify monolayer WS₂ under optical microscope (optical contrast)

8. Dry transfer of monolayer WS₂ on few-layer Graphene via stamping method (the temperature of the Si/SiO₂_Graphene substrate was set to 60°C to promote smoother release of the monolayer WS₂ from PDMS substrate)

9. 30min thermal treatment of the heterostructure Si/SiO₂_Graphene_WS₂ at 150°C (3rd time)

4.3 Spectroscopic study of samples after the annealing treatment

After the annealing procedure described at Section 4.2 a new set of samples was prepared. The characterization of samples B and C was performed right after the annealing treatment. The same standard identification process was carried out for both samples. The image of the new sample B was obtained under optical microscopy (Figure 4.7) and its characterization was made firstly by Raman. This time we proceeded with two Raman spectra (Figure 4.8a, Figure 4.8b) corresponding to two different areas marked by red and blue laser target in Figure 4.7. The reason why we obtain information for two different, yet neighboring areas is to compare the under-examination sample with a known configuration such as Si/SiO₂/WS₂ (area marked by red spot). Apart from a broad mode at around 1000 cm⁻¹ which can be attributed to phonon overtones in Silicon, Raman results for Si/SiO₂/WS₂ area are in a good agreement with those in Figure 4.1. Both E' and A₁' vibrational modes are located at ~360 cm⁻¹ and ~420 cm⁻¹, respectively. Raman spectroscopy of Si/SiO₂/Gr/WS₂ area (blue spot) showed that G and G' graphene modes appeared less intense than those in Figure 4.5b. As previously discussed, decreased intensity might be the first sign of a better coupling between the layers of our heterostructure.

Identification and characterization of sample B

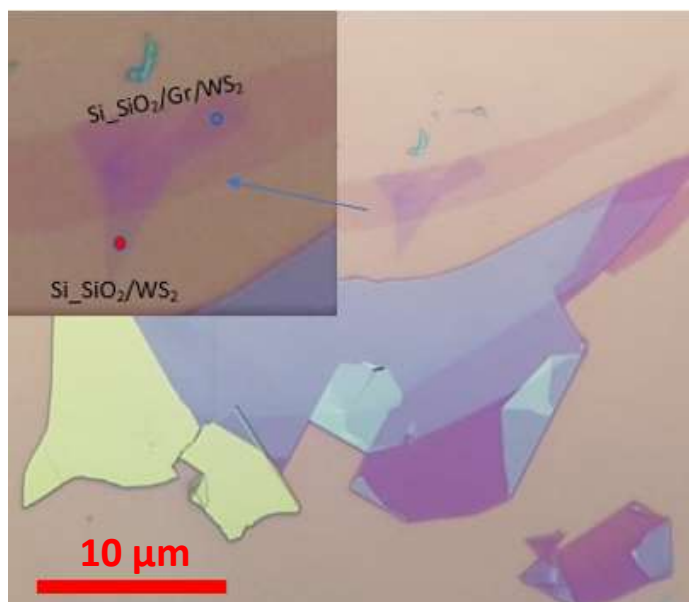


Figure 4.7: Optical microscope image of sample B. The focused area indicates the laser targets corresponding to two different areas of the same sample.

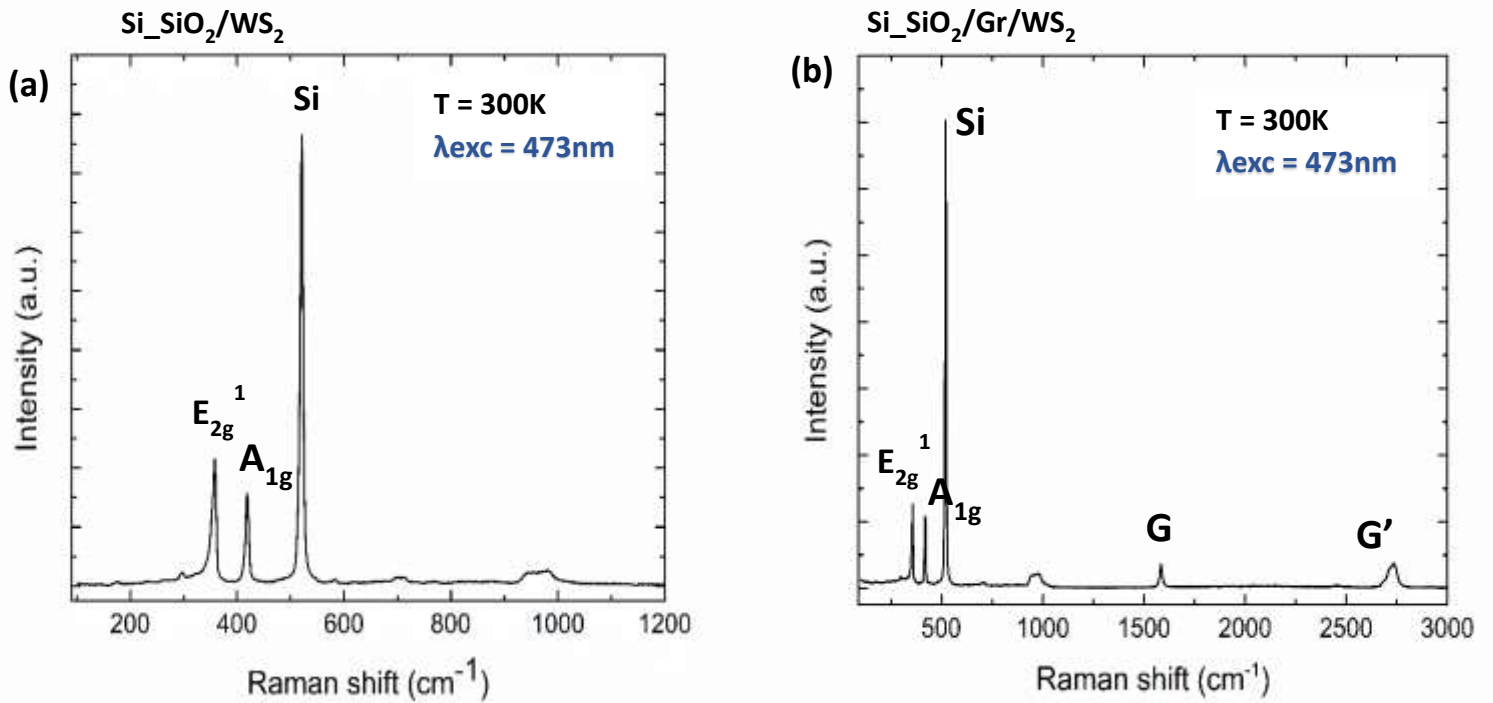


Figure 4.8: Raman spectra of a) Si/SiO₂/WS₂ (red laser target) and b) Si/SiO₂/Gr/WS₂ (blue laser target).

The next step was to continue with Photoluminescence spectroscopy at room temperature. The results for sample B (blue curve) in Figure 4.9 were unambiguous. To start with, there was a tremendous decrease in the PL intensity, comparing to the Si/SiO₂/WS₂ area (red curve) (Figure 4.9a). The “quenching” of the intensity was so significant that we had to multiply by a constant factor of 50 in order to show it in the same figure as the PL of the reference sample. Secondly, a 30 meV red shift was observed which is more clearly depicted in the normalized PL diagram, in Figure 4.9b. This shift is attributed to the presence of underlying graphene that screens the electric field between electrons and holes and leads to a strong reduction in the bandgap and more modest reduction of the exciton binding energy. Last but not least, the overall line shape of the blue curve (sample B) appeared more symmetric and less broad (FWHM = 24 meV) compared to the red curve (FWHM = 44 meV, Si/SiO₂/WS₂). Based on our promising PL results we further carried out a Differential Reflectance investigation of our sample (Figure 4.10). The DR results for sample B showed two prominent peaks at ~1.98 eV and ~2.38 eV for A and B excitons respectively. Furthermore, it is apparent by looking at the red curve that A and B exciton peaks emerge at ~2.01 eV the former and ~2.41 eV the latter, which confirm the red shift for the A- and B-excitons for sample B.

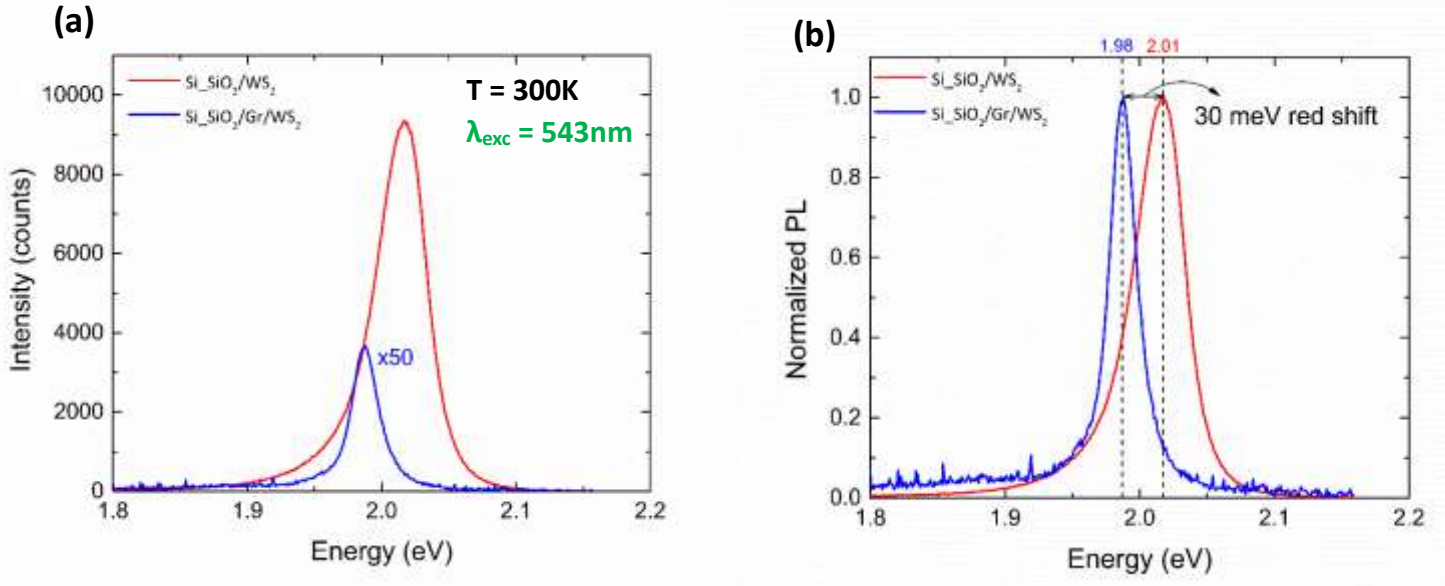


Figure 4.9: a) Photoluminescence of sample B. The red and blue spectra correspond to the laser spots depicted in Figure 4.7. The blue curve was multiplied by a factor of 50 for better visualization and comparison. b) Normalized PL intensity indicating 30 meV red shift for sample B.

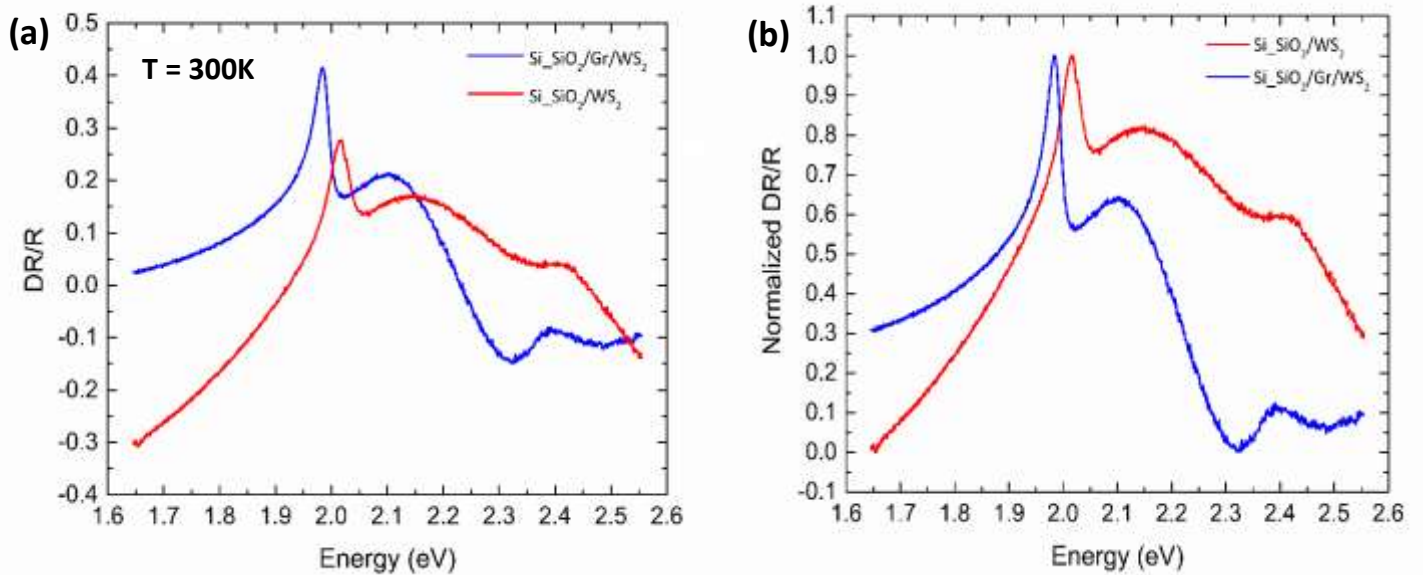


Figure 4.10: a) Differential Reflectance of sample B. The red and blue spectra correspond to the laser spots depicted in Figure 4.7. b) Normalized DR/R in agreement with PL spectra in Figure 4.9.

The optical image of sample C after the annealing treatment is given in Figure 4.11a. The two multilayers of graphene are shown with black arrows. One can observe the strain tensions and even the folding of the graphene layers which remains a challenge during the stacking of such heterostructures. The two areas under investigation are indicated with blue and red arrows. The former is the un-capped sample area with configuration Si/SiO₂/Gr/WS₂, whereas the latter is sample C with the sandwiched configuration Si/SiO₂/Gr/WS₂/Gr. The Raman spectrum in Figure 4.11b completes the characterization of sample C. The Raman modes of our heterostructure remain consistent with our previous findings.

Identification of sample C

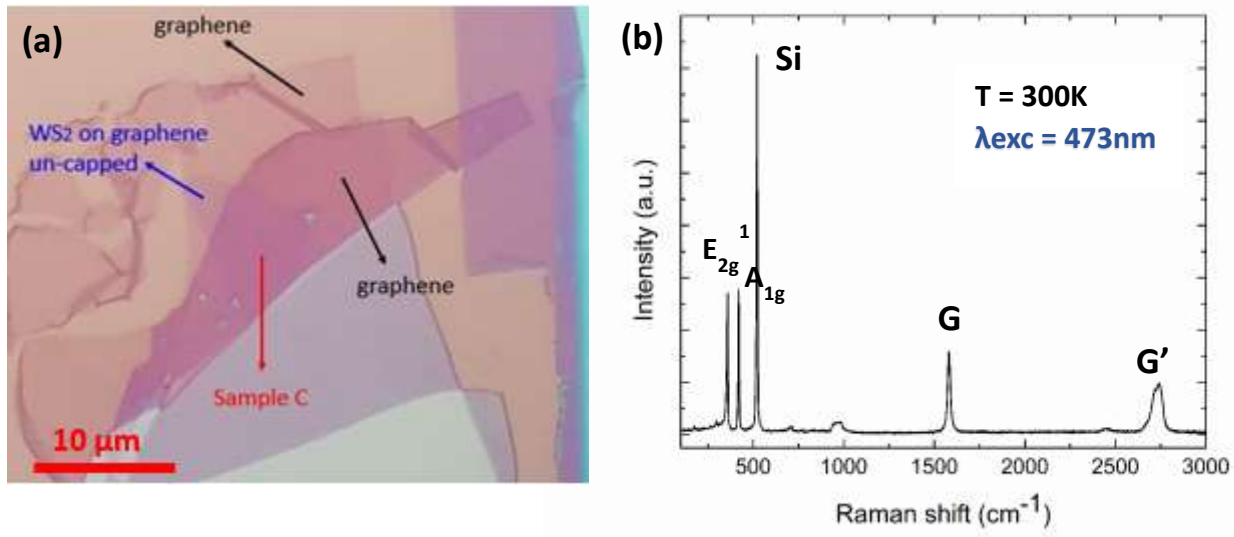


Figure 4.11: a) Optical microscope image of sample C. The red arrow indicates the sandwiched sample area under examination. The blue arrow shows the un-capped area for comparison. b) Raman spectrum of sample C at room temperature.

Photoluminescence results of sample C are consistent comparing to those of sample B. Particularly, in Figure 4.12a the peak corresponding to neutral exciton (~ 1.96 eV) presented a larger red shift compared to the previous one of sample B. Moreover, the exciton peak of the un-capped sample area (blue curve) is at ~ 1.98 eV which is consistent with the results in Figure 4.9 for the same sample configuration. It is also apparent, that PL intensity of sample C experienced an extremely large “quenching” yielding a negligible peak intensity. The normalized PL intensity (Figure 4.12b), had a “noisy” line shape which can be attributed to the large “quenching”. Our current findings proved the development of a specific sample preparation technique which can present a better coupling between the layers of the heterostructure. The importance of the annealing treatment is evident in our spectroscopic study of samples B and C. In Section 4.4, we examine the temperature dependent Photoluminescence of sample C.

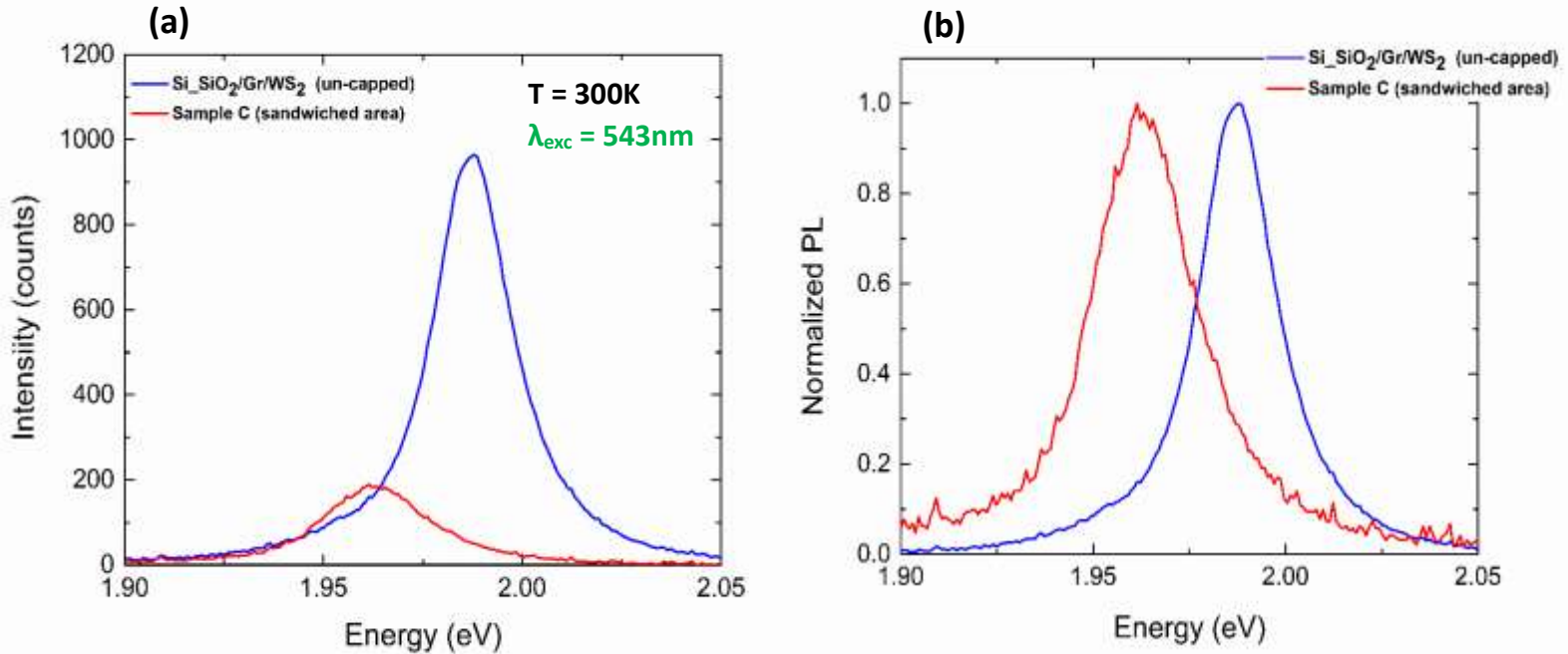


Figure 4.12: Photoluminescence of sample C. a) The red and blue spectra correspond to Sample C and $\text{Si/SiO}_2/\text{graphene/WS}_2$ un-capped area, respectively. b) Normalized PL for the two areas under investigation.

4.4 T-dependent photoluminescence

In this project, we investigated the conditions under which the exfoliated layers could stack, thus forming a well-coupled WS₂/graphene heterostructure. After the annealing treatment the information gathered from the spectroscopic study of our samples presented a large red shift combined with a dramatic drop in PL intensity. The consistency and repetition of our results confirmed that we managed to establish well-coupled heterostructure systems. Therefore, in this section we conducted a temperature dependent PL experiment in order to examine the excitonic behavior of sample C.

The first step was to cool down the sample from room temperature to liquid Nitrogen temperature ($\sim 78\text{K}$). Subsequently, we commenced the analysis with the PL spectrum at 78K. The PL spectrum was comprised of a prominent peak at 2.02 eV, assigned to the neutral A-exciton. On both sides of the neutral exciton peak there are two very weak peaks at $\sim 1.95\text{ eV}$ and $\sim 2.09\text{ eV}$ which correspond to the G'(2D) and G Raman modes of graphene. We further obtained the PL spectra at 100K, 150K, 200K, 250K and 300K under constant laser power. In Figure 4.13 we plot the PL spectra at 78K and 300K for comparison.

Overall, there was a progressive redshift in the exciton emission energies with respect to the rise of temperature. The calculated red shift between the two excitonic positions at 78K and 300K was about 60 meV. This behavior is characteristic of semiconductors and can be explained by considering two contributing mechanisms. Firstly, thermal expansion with increasing temperature leads to an increase in the average interatomic distance, therefore shrinking the relative position of the conduction and valence bands. Nevertheless, the major contribution stems from the renormalization of the electronic energies due to a temperature dependent exciton-phonon interaction [52].

In addition, the maximum PL intensity at 78K (red curve) was about 33% higher compared to PL intensity at 300K (black curve), because carriers drift out of the system when exposed at elevated temperatures [53]. Apart from red shift and “quenching”, the PL spectrum exhibited a wide broadening when reaching at 300K. Full width at Half Maximum (FWHM) was increased from $\sim 0.012\text{ eV}$ to $\sim 0.038\text{ eV}$ for 78K and 300K respectively ($\sim 68\%$ wider). Such broadening of a spectral line can be ascribed mainly to interactions with LO phonons as well as scattering due to impurities and interactions between excitons and acoustic phonons [54].

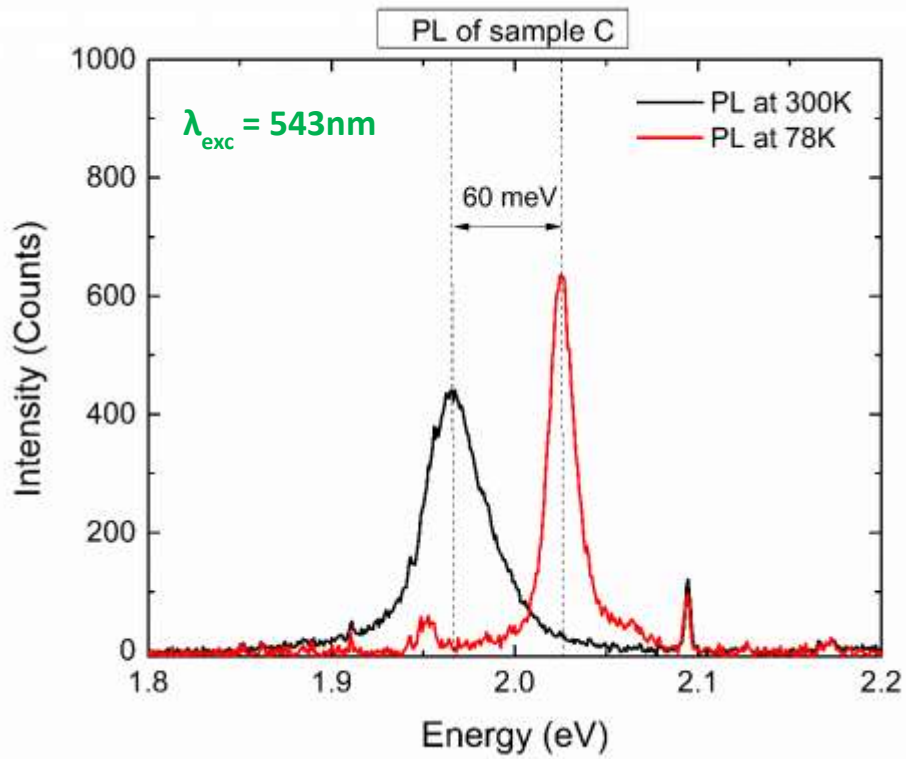


Figure 4.13: Photoluminescence of sample C at 78K (red curve) and 300K (black curve). A prominent red shift of 60 meV is indicated.

From the T-dependent PL data, we can now plot the energy shift of the A-exciton as function of temperature (Figure 4.14). According to literature, the temperature dependent exciton-phonon interaction can be described by the Varshni or O'Donnell relations [53]. Both relations describe the variation of the energy band gap (E_g) with temperature (T).

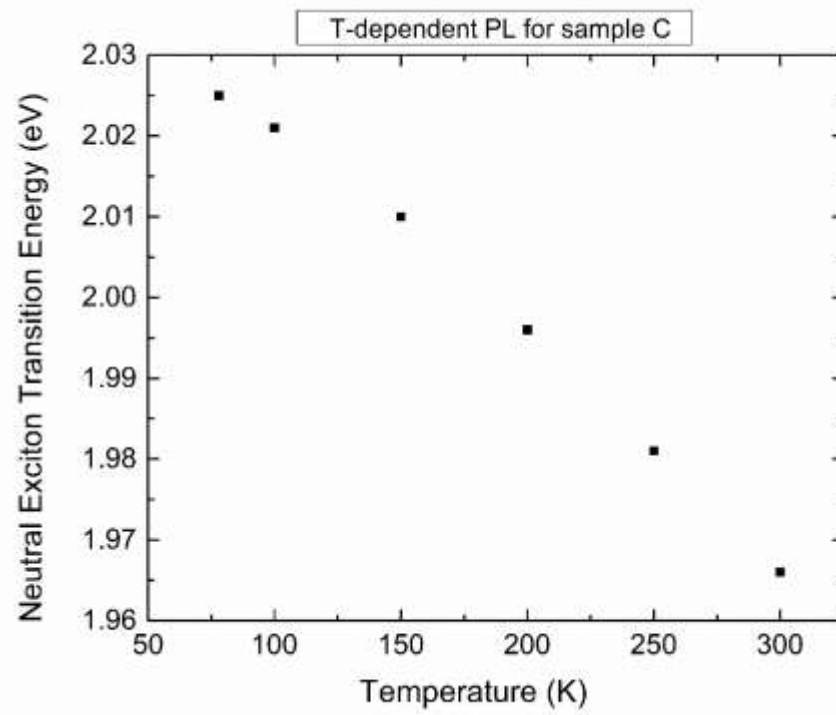


Figure 4.14: Variation of the neutral A exciton transition energy with temperature for sample C.

The main concept of my undergraduate thesis was the spectroscopic studies of WS₂/Graphene heterostructures. The objective was the fabrication and coupling of the WS₂/Graphene heterostructures and the investigation of the effect of few layer-graphene on the optical and electronic properties of monolayer WS₂. The behavior of neutral exciton was examined as function of temperature using standard spectroscopic techniques such as Photoluminescence, Absorbance (Differential Reflectivity) and Raman.

For the characterization of the samples, Raman spectroscopy was used to identify the vibrational modes of the WS₂ monolayer, the few layers of graphene and the final heterostructure system. Micro-photoluminescence and differential reflectivity spectra were collected in a backscattering setup using an excitation source of 543nm continuous wave laser, through a 50x objective lens. Both experimental techniques were also used in combination with the previous Raman measurements to complete the characterization of the samples. A valuable information was gained from the linewidth, the symmetry and the energy position of the excitons through the PL and Reflectivity spectra. The coupling of the heterostructure's layers was investigated by conducting the previous experiments at ambient conditions and room temperature, before and after the annealing process of the structures. Annealing proved to be a significant parameter for the coupling between the layers. Furthermore, the annealed heterostructures were studied as function of temperature and laser power in the range of 78 K to room temperature.

Future studies include spin valley polarization measurements for these heterostructures, in order to probe the effect of the dielectric environment on the initialized polarization, as well as on the depolarization mechanisms.

Part III

References

- [1] G. Yang, L. Li, W. B. Lee, and M. C. Ng, “Structure of graphene and its disorders: a review,” *Science and Technology of Advanced Materials*, vol. 19, no. 1, pp. 613–648, 2018.
- [2] Monisha Chakraborty, Mohammed S. J. Hashmi, *Graphene as a Material – An Overview of Its Properties and Characteristics and Development Potential for Practical Applications*, Materials Science, 2014.
- [3] Supratik Sarkar, “Tunneling in Graphene SymFETs”, Research Gate, 2018.
- [4] Mak, K. F., Lee, C., Hone, J., Shan, J., & Heinz, T. F., “Atomically Thin MoS₂: A New Direct-Gap Semiconductor”, *Physical Review Letters*, 105(13), 2010.
- [5] Hugo Henck, Zeineb Ben Aziza, Debora Pierucci, Feriel Laourine, Francesco Reale, Pawel Palczynski, Julien Chaste, Mathieu G. Silly, François Bertran, Patrick Le Fèvre, Emmanuel Lhuillier, Taro Wakamura, Cecilia Mattevi, Julien E. Rault, Matteo Calandra, and Abdelkarim Ouerghi, “Electronic band structure of Two-Dimensional WS₂/Graphene van der Waals Heterostructures”, *Phys. Rev. B* 97, 155421, 2018.
- [6] Chun xiao, Cong Jingzhi, Shang Xing Wu, Bingchen Cao, Namphung Peimyoo, Caiyu Qiu Litao Sun, Ting Yu, “Synthesis and Optical Properties of Large-Area Single-Crystalline 2D Semiconductor WS₂ Monolayer from Chemical Vapor Deposition”, *Advanced Optical Materials*, Volume2, Issue2, 2013.
- [7] Rou Jun Toh, Zdeněk Sofer, Jan Luxa, David Sedmidubský and Martin Pumera, “3R phase of MoS₂ and WS₂ outperforms the corresponding 2H phase for hydrogen evolution”, *Chemical Communications*, Issue 21, 2017.
- [8] A.T. Hanbicki, G. Kioseoglou, M. Currie, C. Stephen Hellberg, K.M. McCreary, A.L. Friedman & B.T. Jonker, “Anomalous temperature dependent spin-valley polarization in monolayer WS₂”, *Scientific Reports*, 2016.
- [9] Nayak, P. K., Yeh, C.-H., Chen, Y.-C., & Chiu, P.-W., “Layer-Dependent Optical Conductivity in Atomic Thin WS₂ by Reflection Contrast Spectroscopy”, *ACS Applied Materials & Interfaces*, 6(18), 2014.
- [10] Ashwin Ramasubramaniam, “Large excitonic effects in monolayers of molybdenum and tungsten dichalcogenides”, *Phys. Rev. B* 86, 115409, 2012.
- [11] Henck, H., Ben Aziza, Z., Pierucci, D., Laourine, F., Reale, F., Palczynski, P., Ouerghi, A., “Electronic band structure of Two-Dimensional WS₂ /Graphene van der Waals Heterostructures”, *Physical Review B*, 97(15), 2018.

- [12] Piccinini, G., Forti, S., Martini, L., Pezzini, S., Miseikis, V., Starke, Coletti, C., “Deterministic direct growth of WS₂ on CVD graphene arrays”, 2D Materials, 7(1), 014002, 2019.
- [13] Forti, S., Rossi, A., Büch, H., Cavallucci, T., Bisio, F., Sala, A., Coletti, C., “Electronic properties of single-layer tungsten disulfide on epitaxial graphene on silicon carbide” Nanoscale, 9(42), 16412–16419, 2017.
- [14] Yuan, L., Chung, T.-F., Kuc, A., Wan, Y., Xu, Y., Chen, Y. P., Huang, L., “Photocarrier generation from interlayer charge-transfer transitions in WS₂-graphene heterostructures”. Science Advances, 4(2), 2018.
- [15] Cong, C., Shang, J., Wu, X., Cao, B., Peimyoo, N., Qiu, C., Yu, T., “Synthesis and Optical Properties of Large-Area Single-Crystalline 2D Semiconductor WS₂ Monolayer from Chemical Vapor Deposition”, Advanced Optical Materials, 2(2), 131–136, 2013.
- [16] Zhu, B., Chen, X., & Cui, X., “Exciton Binding Energy of Monolayer WS₂”, Scientific Reports, 5(1), 2015.
- [17] Mark Fox, “Optical Properties of Solids” (Oxford Master Series in Condensed Matter Physics), Oxford University Press, 2010.
- [18] Velický, M., & Toth, P. S., “From two-dimensional materials to their heterostructures: An electrochemist’s perspective”, Applied Materials Today, 8, 68–103, 2017.
- [19] Ugeda, M. M., Bradley, A. J., Shi, S.-F., da Jornada, F. H., Zhang, Y., Qiu, D. Y., Crommie, M. F., “Giant bandgap renormalization and excitonic effects in a monolayer transition metal dichalcogenide semiconductor”, Nature Materials, 13(12), 1091–1095, 2014.
- [20] Liu, G.-B., Shan, W.-Y., Yao, Y., Yao, W., & Xiao, D., “*Three-band tight-binding model for monolayers of group-VIB transition metal dichalcogenides*”, Physical Review B, 88(8), 2013.
- [21] Keresztury, G., Raman Spectroscopy: Theory. Handbook of Vibrational Spectroscopy, 2006
- [22] J Michael Hollas, “Modern Spectroscopy”, 4th edition, Wiley Ltd, 2004.
- [23] McCreery, Richard L., Raman spectroscopy for chemical analysis, New York: John Wiley & Sons, INC., Publications, 2000.
- [24] J. R. Ferraro, K. Nakamoto and C. W. Brown, Introductory Raman Spectroscopy, Elsevier, 2003 (Second Edition)

- [25] E. Smith and G. Dent, *Modern Raman Spectroscopy - A Practical Approach*, John Wiley & Sons, Ltd, 2005
- [26] C.V. Raman and K.S. Krishnan, *Nature*, A New Type of Secondary Radiation, 121, 501 (1928)
- [27] Bernath, Peter F. “Spectra of atoms and molecules”, 2005.
- [28] <https://en.wikipedia.org/wiki/Ramanspectroscopy>
- [29] P. Yu, M. Cardona, *Fundamentals of Semiconductors: Physics and Materials Properties*, Springer, (Fourth edition), 2010.
- [30] Molina-Sánchez, A., & Wirtz, L., “Phonons in single-layer and few-layer MoS₂ and WS₂”, *Physical Review B*, 84(15), 2011.
- [31] <https://www.iue.tuwien.ac.at/phd/pourfath/node21.html>
- [32] Ayse Berkdemir, Humberto R. Gutiérrez, Andrés R. Botello-Méndez, Néstor Perea-López, Ana Laura Elías, Chen-Ing Chia, Bei Wang, Vincent H. Crespi, Florentino López-Urías, Jean-Christophe Charlier, Humberto Terrones & Mauricio Terrones, “Identification of individual and few layers of WS₂ using Raman Spectroscopy”, *Scientific Reports*, 2013.
- [33] https://www.cmu.edu/nanotechnology-forum/Forum_12/Presentation/Session-2-2/3%20NSF-KOREA-Oct-5-2015-hterrones-FV.pdf
- [34] Bottari, G., Herranz, M. Á., Wibmer, L., Volland, M., Rodríguez-Pérez, L., Guldi, D. M., Torres, T., “Chemical functionalization and characterization of graphene-based materials”, *Chemical Society Reviews*, 46(15), 4464–4500, 2017.
- [35] Klingshirn, Claus F., “*Semiconductor Optics*”, Springer Verlag, 1995.
- [36] Frisenda, R., Niu, Y., Gant, P., Molina-Mendoza, A. J., Schmidt, R., Bratschitsch, R., Castellanos-Gomez, A., “Micro-reflectance and transmittance spectroscopy: a versatile and powerful tool to characterize 2D materials”, *Journal of Physics D: Applied Physics*, 50(7), 074002, 2017.
- [37] Demtroder W., “*Laser Spectroscopy: Basic Concepts and Instrumentation*”, 3rd Edition, 1981.

- [38] Yue Niu, Sergio Gonzalez-Abad, Riccardo Frisenda, Philipp Marauhn, Matthias Drüppel, Patricia Gant, Robert Schmidt, Najme S. Taghavi, David Barcons, Aday J. Molina-Mendoza, Steffen Michaelis de Vasconcellos, Rudolf Bratschitsch, David Perez De Lara, Michael Rohlfing, Andres Castellanos-Gomez, “Thickness-dependent differential reflectance spectra of monolayer and few-layer MoS₂, MoSe₂, WS₂ and WSe₂”, Journal reference: Nanomaterials, 8, 725, 2018.
- [39] https://en.wikipedia.org/wiki/Absorption_spectroscopy
- [40] Liu, B., Zhao, W., Ding, Z., Verzhbitskiy, I., Li, L., Lu, J., ... Loh, K. P., “*Engineering Bandgaps of Monolayer MoS₂ and WS₂ on Fluoropolymer Substrates by Electrostatically Tuned Many-Body Effects*”, *Advanced Materials*, 28(30), 6457–6464. 2016.
- [41] Zhao, W., Ghorannevis, Z., Chu, L., Toh, M., Kloc, C., Tan, P.-H., & Eda, G., “Evolution of Electronic Structure in Atomically Thin Sheets of WS₂ and WSe₂”, *ACS Nano*, 7(1), 791–797, 2012.
- [42] Ioannis M. Paradisanos, “EXCITONS IN ATOMICALLY THIN TUNGSTEN DISULFIDE (WS₂) LAYERS”, PhD dissertation, 2018.
- [43] Arul, Narayanasamy Sabari, Nithya, “Two Dimensional Transition Metal Dichalcogenides: Synthesis, Properties, and Applications”, 2019.
- [44] Jayasena, B., & Melkote, S. N., “An Investigation of PDMS Stamp Assisted Mechanical Exfoliation of Large Area Graphene”, *Procedia Manufacturing*, 1, 840–853, 2015.
- [45] George Kourmoulakis, “Optical and Electronic Properties of few layers of GeSe”, Master Thesis, 2018.
- [46] Frisenda, R., Navarro-Moratalla, E., Gant, P., Pérez De Lara, D., Jarillo-Herrero, P., Gorbachev, R. V., & Castellanos-Gomez, A., “Recent progress in the assembly of nanodevices and van der Waals heterostructures by deterministic placement of 2D materials”, *Chemical Society Reviews*, 47(1), 53–68, 2018.
- [47] Zhao, W., Ghorannevis, Z., Amara, K. K., Pang, J. R., Toh, M., Zhang, X., Eda, G., “Lattice dynamics in mono- and few-layer sheets of WS₂ and WSe₂”, *Nanoscale*, 5(20), 9677, 2013.
- [48] Jain, A., Bharadwaj, P., Heeg, S., Parzefall, M., Taniguchi, T., Watanabe, K., & Novotny, L., “*Minimizing residues and strain in 2D materials transferred from PDMS*” *Nanotechnology*, 29(26), 265203, 2018.

- [49] Mak, K., He, K., Lee, C. *et al.* Tightly bound trions in monolayer MoS₂. *Nature Mater* **12**, 207–211 (2013)
- [50] Pandey, J., & Soni, A., “Unraveling Biexciton and Excitonic Excited States from Defect Bound States in Monolayer MoS₂”, *Applied Surface Science*, 2018.
- [51] Giusca, C. E., Rungger, I., Panchal, V., Melios, C., Lin, Z., Lin, Y.-C., Kazakova, “*Excitonic Effects in Tungsten Disulfide Monolayers on Two-Layer Graphene*” *ACS Nano*, *10*(8), 7840–7846, 2016.
- [52] Liu, F., Ziffer, M. E., Hansen, K. R., Wang, J., & Zhu, X., “*Direct Determination of Band-Gap Renormalization in the Photoexcited Monolayer MoS₂*”, *Physical Review Letters*, *122*(24), 2019.
- [53] Jagtap, A. M., Khatei, J., & Koteswara Rao, K. S. R., “*Exciton–phonon scattering and nonradiative relaxation of excited carriers in hydrothermally synthesized CdTe quantum dots*”, *Physical Chemistry Chemical Physics*, *17*(41), 27579–27587, 2015.
- [54] Carlo Lamberti & Giovanni Agostini, “*Characterization of Semiconductor Heterostructures and Nanostructures*”, 2nd Edition, 2013.